Computers & Structures Vol. 32, No. 3/4, pp. 563–590, 1989
Printed in Great Britain.

0045-7949/89 $3.00 + 0.00

NONLINEAR ANALYSIS OF CONCRETE STRUCTURES†

KLAUS-JÜRGEN BATHE,‡§ JAN WALCZAK,‖§ ALAN WELCH¶†† and NAGIN MISTRY¶††
‡Massachusetts Institute of Technology, Cambridge, MA 02139, U.S.A.
‖ADINA R & D, Inc., Watertown, MA 02172, U.S.A.
¶Taylor Woodrow Services, Ltd, Middlesex, U.K.

Abstract—Solution capabilities for two- and three-dimensional nonlinear finite element analysis of concrete structures are presented. The concrete material is modeled including the triaxial nonlinear stress–strain behavior, tensile cracking, tension-stiffening, compression crushing and strain-softening. The results of various sample analyses are given to demonstrate the constitutive model and the solution strategies. These analyses include the response predictions of a test beam and of small scale models of two reactor vessels.

1. INTRODUCTION

During recent years, interest in nonlinear analysis of concrete structures has increased steadily, because of the wide use of plain, reinforced and prestressed concrete as a structural material, and because of the development of relatively powerful finite element procedures [1]. If a realistic nonlinear analysis of a concrete structure can be carried out, the safety of the structure is increased and the cost can frequently be reduced.

Concrete exhibits a complex structural response with various important nonlinearities; namely, a nonlinear stress–strain behavior, tensile cracking and compression crushing material failures and temperature-dependent creep strains [2–9]. All these concrete nonlinearities depend strongly on the triaxial state of stress, and in addition the nonlinearities introduced by reinforcing and prestressing steel should in general be taken into account [10–13].

There are a number of factors that have prevented the wider acceptability of nonlinear finite element analysis procedures in the analysis of concrete structures. A first important consideration is that the constitutive properties of concrete have not as yet been identified completely, and there is still no generally accepted material law available to model concrete behavior. A second important factor is that nonlinear finite element analysis of concrete structures can be very costly and may require considerable user expertise. The high cost of nonlinear analysis of concrete structures is largely due to the difficulties encountered in the stability and accuracy of the solutions. These difficulties, however, are a direct consequence of the specific numerical implementation of the concrete nonlinearities.

The objective in this paper is to present the three-dimensional concrete model available in ADINA and show some applications. The concrete model was in many respects already proposed in [2]. However, our recent improvements on the model have been very significant and promise to make the model much more attractive for practical nonlinear concrete analyses.

Although we could have chosen to present only our recent improvements on the concrete model, we believe that it is of more interest to have the complete model description in this paper with applications.

The basic aim in the development of the model was to implement in ADINA a model that with the present constitutive descriptions, numerical methods and computing equipment available would satisfy the following two criteria. Firstly, the model should be as simple as possible, but reproduce the important nonlinear and strength characteristics consistent with experimental results. Secondly, the model should be theoretically sound and numerically stable, so that reliable analysis results are obtained.

The material model is a hypoelastic model based on a uniaxial stress–strain relation that is generalized to take biaxial and triaxial stress conditions into account. Tensile cracking and compression crushing conditions are identified using failure surfaces, and strain-softening effects are included in the compression and the tensile regions. A particularly valuable property of the model is that it is defined by a number of input parameters that provide considerable flexibility in its use (and indeed the model may also be employed to model sand or rock structures).

In the following sections we first present the concrete model in detail. We then give some small-size applications, merely to demonstrate the details of the model behavior when it is subjected to various stress–strain paths. Finally, in Part II of the paper we present the results of the analyses of the Sandia pressure vessel, an alkali–silica reacted beam and a PWR prestressed concrete containment. The solution

† Original figures were generated with a colour producing terminal and submitted in colour.
§ Co-author of Part I.
†† Co-author of Part II.

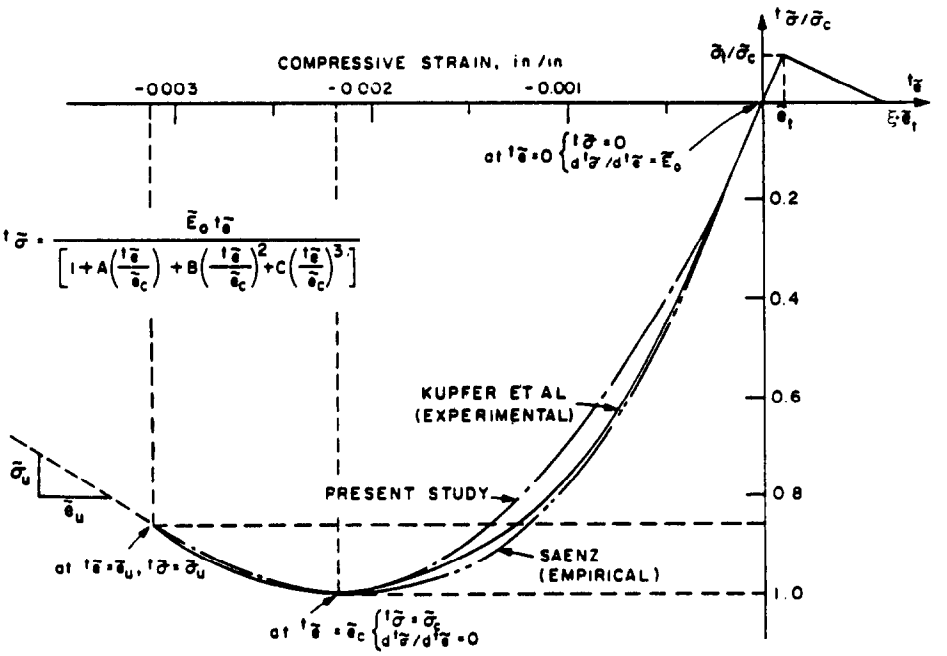

Fig. 1. Concrete model uniaxial stress–strain law.

results presented in this section are particularly valuable because they can be compared with and interpreted against laboratory experimental results.

An important issue in nonlinear analysis is the visualization of the obtained response predictions. In this paper we use our standard post-processing program ADINA-PLOT to present all of our solution results.

2. PART I: THE CONCRETE MATERIAL MODEL

The model implemented employs three basic features to describe the material behavior, namely (i) a nonlinear stress–strain relation including strain-softening to allow for the weakening of the material in compression, (ii) failure envelopes that define cracking in tension and crushing in compression, and (iii) a strategy to model the post-cracking and crushing behavior of the material. In the solution, the material can be subjected to cyclic loading conditions, i.e. the numerical solution allows for unloading and reloading including deactivation of tensile failures. However, as will become apparent, the cyclic loading conditions are only modeled realistically in situations of essentially proportional loading.

In the following, the material model is described for infinitesimal displacement conditions using the engineering stresses ${}^t\sigma_{ij}$ and engineering strains ${}^te_{ij}$. In order to analyze problems with large rotation conditions, the total Lagrangian stress and strain variables must be substituted for the engineering variables [1], and then the model is directly applicable.†

† We use the notation of Refs [1,2] in this paper.

2.1. *Stress–strain relations*

The general multiaxial stress–strain relations are derived from a uniaxial stress–strain relation ${}^t\tilde{\sigma}$ versus ${}^t\tilde{e}$. In this section, we describe the uniaxial and multiaxial stress–strain relations employed in the model and concentrate on the behavior prior to tensile cracking or compression crushing.

In the following discussion, all uniaxial parameters are identified by a tilde (~) placed over them (i.e. all parameters that have been obtained from Fig. 1 carry a tilde).

2.1.1. *Uniaxial conditions.* A typical uniaxial stress, ${}^t\tilde{\sigma}$, to uniaxial strain, ${}^t\tilde{e}$, relation (assuming continuous loading of the material) is shown in Fig. 1 [6]. This stress–strain relation shows that there are basically four strain phases; namely, corresponding to $\tilde{e}_t > {}^t\tilde{e} \geqslant 0$, $\tilde{e}_m \geqslant {}^t\tilde{e} \geqslant \tilde{e}_t$, $0 > {}^t\tilde{e} \geqslant \tilde{e}_c$ and $\tilde{e}_c > {}^t\tilde{e} \geqslant \tilde{e}_u$, where $\tilde{e}_t$ is the strain corresponding to the uniaxial cut-off tensile stress $\tilde{\sigma}_t$, $\tilde{e}_m$ is equal to $\xi \cdot \tilde{e}_t$, where ξ is an input parameter, $\tilde{e}_c$ is the strain corresponding to the minimum (crushing) stress, $\tilde{\sigma}_c$, that can be reached, and $\tilde{e}_u$ is the ultimate compressive strain. If $\tilde{e}_t \geqslant {}^t\tilde{e} > 0$, i.e. the material is in tension, the stress–strain relation is linear until tensile failure at the stress $\tilde{\sigma}_t$, and a constant Young's modulus $\tilde{E}_0$ is employed,

$$ {}^t\tilde{\sigma} = \tilde{E}_0 {}^t\tilde{e} \tag{1} $$

$$ \frac{\mathrm{d}\,{}^t\tilde{\sigma}}{\mathrm{d}\,{}^t\tilde{e}} = \tilde{E}_0. \tag{2} $$

For ${}^t\tilde{e} \leqslant 0$, we assume the following relation,

$$ {}^t\tilde{\sigma}/\tilde{\sigma}_c = \frac{(\tilde{E}_0/\tilde{E}_s)({}^t\tilde{e}/\tilde{e}_c)}{1 + A({}^t\tilde{e}/\tilde{e}_c) + B({}^t\tilde{e}/\tilde{e}_c)^2 + C({}^t\tilde{e}/\tilde{e}_c)^3} \tag{3} $$

and hence,

$$ {}^{t}\tilde{E} = \frac{\tilde{E}_0[1 - B({}^{t}\tilde{e}/\tilde{e}_c)^2 - 2C({}^{t}\tilde{e}/\tilde{e}_c)^3]}{[1 + A({}^{t}\tilde{e}/\tilde{e}_c) + B({}^{t}\tilde{e}/\tilde{e}_c)^2 + C({}^{t}\tilde{e}/\tilde{e}_c)^3]^2} \quad (4) $$

where

$$ A = \frac{\tilde{E}_0/\tilde{E}_u + (p^3 - 2p^2)\tilde{E}_0/\tilde{E}_s - (2p^3 - 3p^2 + 1)}{(p^2 - 2p + 1)p} $$

$$ B = (2\tilde{E}_0/\tilde{E}_s - 3) - 2A, \quad C = (2 - \tilde{E}_0/\tilde{E}_s) + A $$

and the strength parameters $\tilde{E}_0$, $\tilde{\sigma}_c$, $\tilde{e}_c$, $\tilde{E}_s = \tilde{\sigma}_c/\tilde{e}_c$, $\tilde{\sigma}_u$, $\tilde{e}_u$, $p = \tilde{e}_u/\tilde{e}_c$ and $\tilde{E}_u = \tilde{\sigma}_u/\tilde{e}_u$ are obtained from uniaxial tests. It may be difficult to determine somewhat accurate values of $\tilde{\sigma}_u$ and $\tilde{e}_u$, in which case reasonable values should be assumed by the analyst.

The stress–strain relation in eqn (3) assumes monotonic loading conditions. For unloading conditions and loading back to the stress state from which unloading occurred, the initial Young's modulus $\tilde{E}_0$ is used. For strain states beyond $\tilde{e}_u$ in compression, it is usually assumed that the material cannot resist any load and the stresses are set to zero. However, an option for a gradual stress unloading beyond $\tilde{e}_u$ is also included.

mined,

$$ {}^{t}f < f_{\max} \quad (6) $$

where $f_{\max}$ is the maximum value of the loading function that has been reached during the complete solution. In unloading, the initial Young's modulus, $\tilde{E}_0$, is used to form the incremental stress–strain matrix, both for stiffness and stress calculations.

To obtain the stress–strain relations in loading conditions, the principal stresses are calculated and for each principal stress direction a uniaxial tangent Young's modulus, ${}^{t}\tilde{E}_{pi}$, corresponding to the strain in the principal stress direction, ${}^{t}e_{pi}$, is evaluated using eqns (2) and (4). When using eqn (4), the current strain ${}^{t}e_{pi}$ is employed and to account for multiaxial stress conditions the material variables $\tilde{\sigma}_c$, $\tilde{\sigma}_u$, $\tilde{e}_c$ and $\tilde{e}_u$ are replaced by the variables $\tilde{\sigma}_c'$, $\tilde{\sigma}_u'$, $\tilde{e}_c'$ and $\tilde{e}_u'$ defined in eqns (13) and (14).

Let ${}^{t}\sigma_{p1}$, ${}^{t}\sigma_{p2}$ and ${}^{t}\sigma_{p3}$ be the principal stresses at time t, with ${}^{t}\sigma_{p3} \leqslant {}^{t}\sigma_{p2} \leqslant {}^{t}\sigma_{p1}$ and ${}^{t}\tilde{E}_{p1}$, ${}^{t}\tilde{E}_{p2}$ and ${}^{t}\tilde{E}_{p3}$ the corresponding uniaxial Young's moduli. Hence, the material is considered as orthotropic with the directions of orthotropy defined by the principal stresses. The stress–strain matrix corresponding to these directions is, considering three-dimensional stress conditions,

$$ \mathbf{C} = \frac{1}{(1+\nu)(1-2\nu)} \begin{bmatrix} (1-\nu){}^{t}\tilde{E}_{p1} & \nu\,{}^{t}E_{12} & \nu\,{}^{t}E_{13} & 0 & 0 & 0 \\ & (1-\nu){}^{t}\tilde{E}_{p2} & \nu\,{}^{t}E_{23} & 0 & 0 & 0 \\ & & (1-\nu){}^{t}\tilde{E}_{p3} & 0 & 0 & 0 \\ & & & \tfrac{1}{2}(1-2\nu){}^{t}E_{12} & 0 & 0 \\ & \text{symmetric} & & & \tfrac{1}{2}(1-2\nu){}^{t}E_{13} & 0 \\ & & & & & \tfrac{1}{2}(1-2\nu){}^{t}E_{23} \end{bmatrix} \quad (7) $$

2.1.2. *Multiaxial conditions.* The behavior of concrete under multiaxial stress conditions is very complex and has not been assessed experimentally in a complete manner. Various material models with considerable simplifying assumptions have been proposed in the literature. Considering the variability of concrete materials that need be described in practice, the objective in this work was to develop an effective but simple model that provides sufficient flexibility to the analyst to fit the basic material behavior.

The stress–strain relations are evaluated differently depending on whether the material is loading or unloading.

To characterize loading and unloading conditions we define a loading function ${}^{t}f$,

$$ {}^{t}f = {}^{t}\bar{s} \quad (5) $$

where ${}^{t}\bar{s} = (\frac{1}{2}{}^{t}s_{ij}{}^{t}s_{ij})^{1/2}$, ${}^{t}s_{ij} = {}^{t}\sigma_{ij} - {}^{t}\sigma_m\delta_{ij}$, ${}^{t}\sigma_m = 1/3\,{}^{t}\sigma_{ii}$, and δ_{ij} is the Kronecker delta. The material is loading except when the unloading conditions are determined,

where ν is the Poisson ratio, and the shear modulus in a coordinate plane is calculated from the weighted Young's modulus corresponding to that plane,

$$ {}^{t}G_{ij} = \frac{{}^{t}E_{ij}}{2(1+\nu)} = \frac{1}{2(1+\nu)} \frac{|{}^{t}\sigma_{pi}|\,{}^{t}\tilde{E}_{pi} + |{}^{t}\sigma_{pj}|\,{}^{t}\tilde{E}_{pj}}{|{}^{t}\sigma_{pi}| + |{}^{t}\sigma_{pj}|}. \quad (8) $$

The above stress–strain relations for material loading conditions are only employed in the calculation of the stiffness matrix at time t. Considering the evaluation of the stress increment, $\boldsymbol{\sigma}$, from time t to time $t + \Delta t$, the stress integration is approximated in the following manner,

$$ \boldsymbol{\sigma} = \bar{\mathbf{C}}\mathbf{e} \quad (9) $$

where $\mathbf{e}$ is the strain increment. The stress–strain matrix $\bar{\mathbf{C}}$ is as $\mathbf{C}$ in eqn (7) but the uniaxial Young's moduli ${}^{t}\tilde{E}_{pi}$ are replaced by the moduli ${}^{\tau}\tilde{E}_{pi}$. These are evaluated using the uniaxial stress–strain relationship

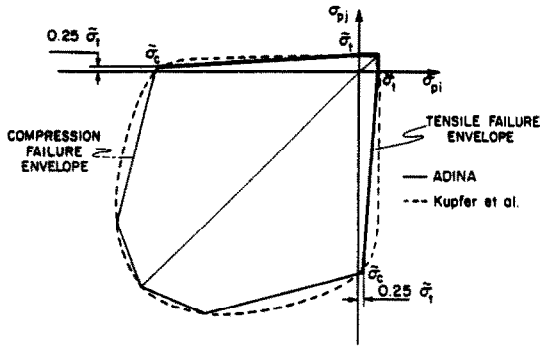

Fig. 2. Triaxial failure envelopes reduced to two-dimensional conditions.

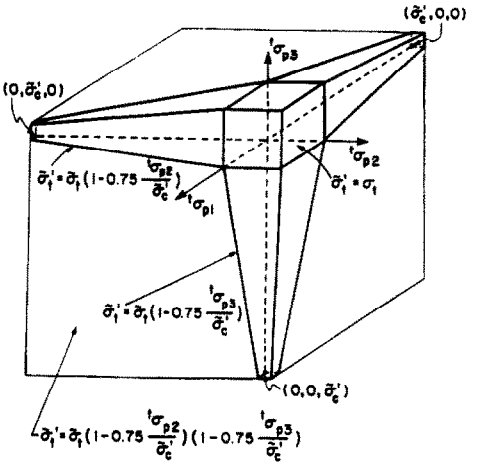

Fig. 3. Triaxial tensile failure envelope.

in Fig. 1, namely, for ${}^{t}\sigma_{pi} \geq 0$ we have

$$ {}^{\tau}\tilde{E}_{pi} = \tilde{E}_0 \tag{10} $$

and if ${}^{t}\sigma_{pi} < 0$, we define

$$ {}^{t+\Delta t}\sigma'_{pi} = \frac{\tilde{E}_0 \cdot {}^{t+\Delta t}e_{pi}}{\left[1 + A\left(\frac{{}^{t+\Delta t}e_{pi}}{\tilde{e}'_c}\right) + B\left(\frac{{}^{t+\Delta t}e_{pi}}{\tilde{e}'_c}\right)^2 + C\left(\frac{{}^{t+\Delta t}e_{pi}}{\tilde{e}'_c}\right)^3\right]} \tag{11} $$

and then

$$ {}^{t+\Delta t}\tilde{E}_{pi} = \frac{{}^{t+\Delta t}\sigma'_{pi} - {}^{t}\sigma_{pi}}{{}^{t+\Delta t}e_{pi} - {}^{t}e_{pi}}. \tag{12} $$

Here, ${}^{t+\Delta t}e_{pi}$ and ${}^{t}e_{pi}$ are the strain components at time $t + \Delta t$ and t in the directions of the principal stresses.

2.2. *Material failure envelopes*

To model the failure of the material in tension and compression in two- and three-dimensional analysis and to account for multiaxial conditions in the uniaxial stress–strain law of Fig. 1, failure envelopes are employed. Figure 2 shows an example of the failure envelopes used corresponding to two principal stress directions. Regarding the tensile failure it is noted that considering one principal stress direction the tensile strength of the material in this direction does not change with the introduction of a tensile stress in the other principal stress direction, but a compressive stress decreases this tensile strength.

The failure envelopes shown in Fig. 2 are a special case of the triaxial failure envelopes for tensile and compressive failures shown in Figs 3 and 4.

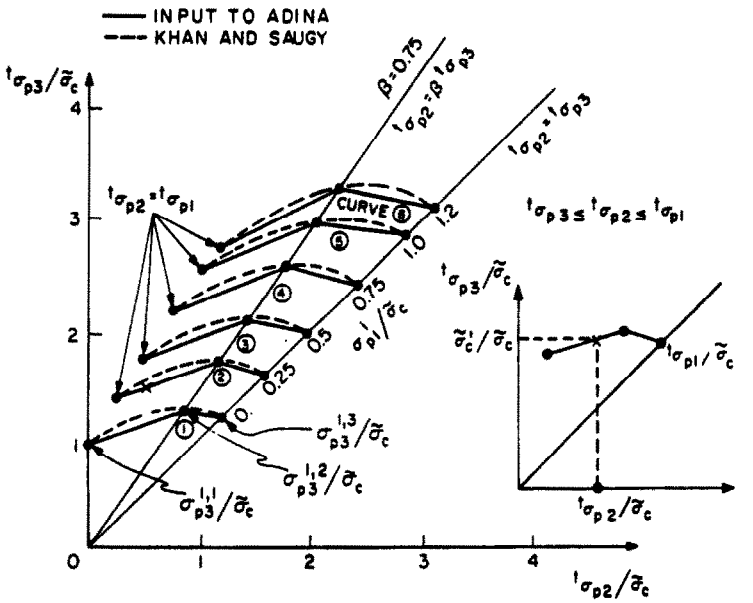

Fig. 4. Triaxial compression failure envelope.

The triaxial tensile failure envelope is a straightforward generalization of the envelope for two-dimensional analysis. However, the compressive failure envelope is more complex and requires more data input. The envelope can be used to represent a large number of different envelopes like the biaxial envelope of Liu *et al.* [7] and the triaxial failure surface of Khan and Saugy [8]. The shape of the compressive failure surface used is largely based on the experimental results reported by Kupfer *et al.* [6] and Launay and Gachon [9].

The compressive failure envelope is input using 24 discrete stress values. Firstly, the values $\sigma^i_{p1}/\tilde{\sigma}_c$ are input. These values define at what stress magnitudes ${}'\sigma_{p1}$ the discrete two-dimensional failure envelopes for additional stresses ${}'\sigma_{p2}$ and ${}'\sigma_{p3}$ are input. These failure envelopes are defined by the failure stress values $\sigma^{ij}_{p3}/\tilde{\sigma}_c$ ($i = 1, \ldots, 6; j = 1, 2, 3$) that correspond to the stress magnitudes ${}'\sigma_{p2} = {}'\sigma_{p1}$, ${}'\sigma_{p2} = \beta\,{}'\sigma_{p3}$ (β is a constant) and ${}'\sigma_{p2} = {}'\sigma_{p3}$.

The failure envelopes are employed to establish the uniaxial stress–strain law accounting for multiaxial stress conditions, and to identify whether tensile or crushing failure of the material has occurred. Having calculated the current principal stresses, to establish the uniaxial stress–strain law it is assumed that ${}'\sigma_{p1}$ and ${}'\sigma_{p2}$ are held constant and the minimum stress that would have to be reached in the third principal stress direction to cause crushing of the material is calculated using the failure envelopes (see Fig. 4). Let this stress be $\tilde{\sigma}'_c$ and $\gamma_1 = \tilde{\sigma}'_c/\tilde{\sigma}_c$, then we also use

$$\tilde{\sigma}'_u = \gamma_1 \tilde{\sigma}_u \tag{13}$$

$$\tilde{\varepsilon}'_c = (C_1\gamma_1^2 + C_2\gamma_1)\tilde{\varepsilon}_c; \quad \tilde{\varepsilon}'_u = (C_1\gamma_1^2 + C_2\gamma_1)\tilde{\varepsilon}_u \tag{14}$$

where C_1 and C_2 are constants defined by the user; normally, $C_1 = 1.4$ and $C_2 = -0.4$. The constants $\tilde{\sigma}'_c, \tilde{\sigma}'_u, \tilde{\varepsilon}'_c, \tilde{\varepsilon}'_u$ are employed instead of the unprimed variables in order to establish, using eqn (4), the uniaxial stress–strain law under multiaxial conditions (see Fig. 5).

To identify whether the material has failed, the principal stresses are used to locate the current stress state in the failure envelopes. In the following we consider how one single plane of tensile failure develops and how the material fails in compression crushing.

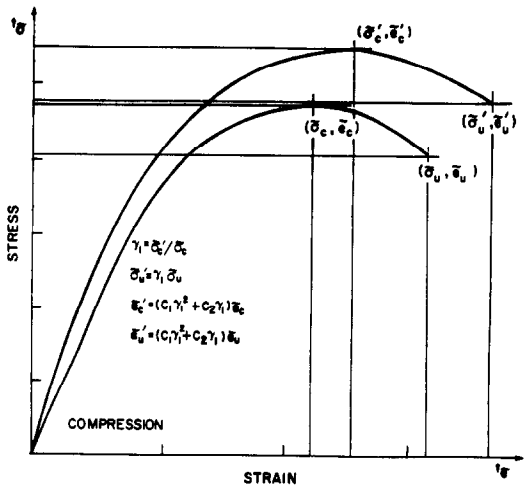

Fig. 5. Increase of strength parameters for model under multiaxial conditions.

Tensile failure occurs if the tensile stress in a principal stress direction exceeds the tensile failure stress. In this case it is assumed that a plane of failure develops perpendicular to the principal stress direction. The effect of this material failure is that the normal and shear stiffnesses across the plane of failure, and the corresponding normal stress and shear stresses, are reduced.

Prior to tensile failure the stress–strain material law is given by eqns (7)–(12). Assuming that ${}'\sigma_{p1}$ is larger than the tensile failure stress, the new material stress–strain matrix is in the stiffness matrix calculation,

$$\mathbf{C} = \begin{bmatrix} {}'\tilde{E}_0\eta_n & 0 & 0 & 0 & 0 & 0 \\ & \dfrac{1}{1-\nu^2}\begin{bmatrix} {}'\tilde{E}_{p2} & \nu\,{}'E_{23} \\ & {}'\tilde{E}_{p3} \end{bmatrix} & & 0 & 0 & 0 \\ & & & 0 & 0 & 0 \\ & & & \dfrac{\tilde{E}_0\eta_s}{2(1+\nu)} & 0 & 0 \\ & \text{symm.} & & & \dfrac{\tilde{E}_0\eta_s}{2(1+\nu)} & 0 \\ & & & & & \dfrac{{}'E_{23}}{2(1+\nu)} \end{bmatrix}, \tag{15}$$

where the ${}'\tilde{E}_{pi}$ are the uniaxial Young's moduli evaluated in the principal stress directions using eqns (2) and (4) and the ${}'E_{ij}$ are evaluated using eqn (8). The constant η_n is a small value, normally 10^{-4}, to reduce the stiffness normal to the tensile failure plane, and the constant η_s, normally 0.5, reduces the shear stiffness in the tensile failure plane.

For the stress calculation, the following stress–strain matrices are used.

For the tensile stress normal to the tensile failure plane and the shear stresses in this plane, we use the total strains to calculate the total stresses with

$$\tilde{\mathbf{C}} = \begin{bmatrix} E_f & 0 & 0 \\ & G_{12}^f & 0 \\ \text{symm.} & & G_{13}^f \end{bmatrix} \tag{16}$$

where E_f and G_{12}^f, G_{13}^f are evaluated as shown in Fig. 6. In this figure ξ is a variable, input by the user, that defines the amount of tension stiffening. Figure 6 shows that G_{ij}^f is a fraction of the initial shear modulus, $\tilde{E}_0/2(1+\nu)$, corresponding to the total strain normal to the tensile failure plane. Also, Fig. 6 assumes loading from zero stress directly into the tensile region. If the tensile stress is reached by unloading from a compressive stress, the strain normal to the tensile failure plane is measured from the strain at which the stress is zero (see the example of Fig. 7).

For the remaining stress components, the increment in the stresses is evaluated from the incremental strains using

$$\tilde{\mathbf{C}} = \frac{1}{1-\nu^2} \begin{bmatrix} {}^{\tau}\tilde{E}_{p2} & \nu\,{}^{\tau}E_{23} & 0 \\ & {}^{\tau}\tilde{E}_{p3} & 0 \\ \text{symm.} & & (1-\nu^2)\,{}^{\tau}G_{23} \end{bmatrix} \tag{17}$$

where the ${}^{\tau}\tilde{E}_{pi}$ are the uniaxial Young's moduli evaluated using eqn (12) and ${}^{\tau}E_{23}$ and ${}^{\tau}G_{23}$ are evaluated using eqn (8) but with ${}^{\tau}\tilde{E}_{pi}$ instead of ${}^{t}\tilde{E}_{pi}$.

Considering eqns (15), (16) and (17), we note that by use of eqn (16) the tensile stress normal to the tensile failure plane and the shear stresses in this plane are gradually released. Also, the equations show that plane stress conditions are assumed to exist at the plane of tensile failure. The factor η_n is not set exactly equal to zero in order to avoid the possibility of a singular stiffness matrix. The value to be employed for η_s must depend on a number of physical factors, and in the numerical solution it is at this time best to leave η_s as a variable that is input by the analyst.

For visualization, the 'plane of tensile failure' is referred to as a 'crack', but we should interpret this terminology judiciously because a physical crack does not actually develop at the element integration point. Instead, the material has failed in one principal stress direction.

Equations (15), (16) and (17) describe the solution when tensile failure occurs. To identify compression failure, the largest principal stress ${}^{t}\sigma_{p1}$ is employed to establish from Fig. 4 by interpolation, the biaxial failure envelope on ${}^{t}\sigma_{p2}$ and ${}^{t}\sigma_{p3}$. The material has crushed if the stress state corresponding to ${}^{t}\sigma_{p2}$ and ${}^{t}\sigma_{p3}$ lies on or outside the biaxial failure envelope.

2.3. *Post-tensile cracking behavior*

Once a tensile plane of failure has formed, it is checked in each subsequent solution step whether the failure is still active. The failure is considered to be inactive provided the normal strain across the plane becomes negative and less than the strain at which the 'last' failure occurred and is active otherwise. Therefore, a tensile failure plane may repeatedly be active and inactive.

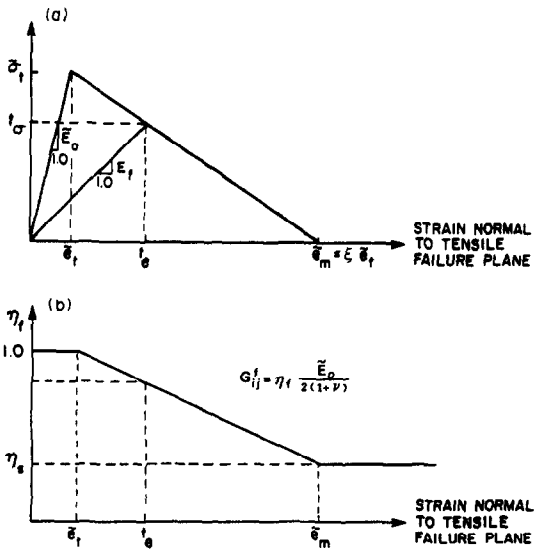

Fig. 6. Material moduli for stress calculation under tensile failure. (a) Calculation of Young's modulus E_f, normal to tensile failure plane. (b) Calculation of shear modulus in tensile failure plane.

If a tensile failure plane has developed, which may or may not be active, the material stress–strain relations are always established as described above but corresponding to the principal stress directions in the failure plane and the direction perpendicular to this plane. Hence, instead of using the principal stresses and corresponding directions as done for the unfailed material, the stress conditions along and normal to the material tensile failure plane are used to evaluate the stress–strain matrix. Also, when a failure plane is or was active, a subsequent failure plane is assumed to form perpendicular to the direction of the one that developed first, once a normal stress along the original failure plane has reached the tensile failure stress. It follows that at any integration point, the direction of the third tensile failure plane is fixed once failure has occurred in two directions.

It may also happen that after tensile failure of the material (in one or two directions) the material fails in compression crushing, which is identified, as usual, by entering the compression crushing envelope in Fig. 4 with the principal stress(es) that act(s) along the tensile failure plane(s).

If the material has crushed in compression, it is assumed that the material strain-softens into all directions.

2.4. *Post-compression crushing, strain-softening behavior*

Consider first uniaxial stress conditions. As shown in Fig. 1, for a uniaxial strain smaller than $\tilde{\varepsilon}_c$, the

material has crushed and softens with increasing compressive strain, i.e. ${}^{t}\tilde{E}$ is negative.

Under multiaxial stress conditions the compression crushing is identified using the multiaxial failure envelope, and once the material has crushed isotropic conditions are assumed using the uniaxial stress–strain law with the constants $\tilde{\sigma}_c'$, $\tilde{e}_c'$ and so on (see Fig. 5) corresponding to the multiaxial conditions at crushing. The Young's modulus for the isotropic material law is evaluated using

$$ {}^{t}\tilde{E} = [\tilde{\sigma}\,|_{at\ {}^{t}e_{p3}+e_{p3}} - \tilde{\sigma}\,|_{at\ {}^{t}e_{p3}}]/e_{p3} \tag{18} $$

where ${}^{t}e_{p3}$ and e_{p3} are the strain component and incremental strain component at time t measured in the direction of the principal stress ${}^{t}\sigma_{p3}$.

Note that, as shown in Fig. 1, when ${}^{t}e_{p3}$ becomes equal to or less than $\tilde{e}_u'$, the stresses are set to zero. However, an option is available for a gradual stress unloading in which case the constant Young's modulus $\tilde{E}_u = -\tilde{\sigma}_u'/\tilde{e}_u'$ is employed, i.e. in eqn (18) we then use ${}^{t}\tilde{E} = \tilde{E}_u$.

If unloading of the crushed material in the strain-softening region occurs characterized by $e_{p3} \geq 0$, the initial Young's modulus $\tilde{E}_0$ is used. In all these calculations the principal stresses are checked individually whether a positive value has been reached, and if so, the stress in the corresponding direction is set to zero.

2.5. *Poisson's ratio in the compressive region*

It has been observed in experiments that the ratio of lateral strain to principal compressive strain remains constant until approximately 80% of the maximum compressive stress $\tilde{\sigma}_c$.

Usually we assume in our analyses that the Poisson ratio is constant; however, as an option a value, v_S, can be used when the material dilates under compression. The value of v_S is given by [10],

$$ v_S = v \quad \text{when } \gamma_2 = \frac{{}^{t}\sigma_{p3}}{\tilde{\sigma}_c'} \leq \gamma_a $$

$$ v_S = v_f - (v_f - v)\sqrt{\left[1 - \left(\frac{\gamma_2 - \gamma_a}{1 - \gamma_a}\right)^2\right]} \quad \text{when } \gamma_2 > \gamma_a \tag{19} $$

where v is the initial Poisson's ratio, v_f is the maximum value of Poisson's ratio at failure and γ_a is usually set to 0.8.

2.6. *Temperature effects*

In some analyses temperature strains, ${}^{t}\mathbf{e}^{th}$, need to be included. These strains are taken into account by replacing the total incremental strain, $\mathbf{e}$, in the governing incremental equations by the strain $\mathbf{e} - \mathbf{e}^{th}$, where $\mathbf{e}^{th}$ is the thermal incremental strain and is calculated from the temperature conditions.

2.7. *Example solutions*

In the following, we present some simple, small-size applications to demonstrate the details of the model behavior when it is subjected to various load conditions. In all these examples a constant Poisson ratio v is used.

Figure 7 summarizes the response obtained when subjecting a single plane stress element to biaxial strain-controlled loading. This solution includes initiation, closing and reopening of a crack; loading, unloading and reloading with large load steps; and crushing of the material with strain-softening behavior. In this figure, the numbers indicate load steps in the analysis. Note that the material model can be used with relatively large load step increments. Figure 8 shows the material failure for different load steps indicated in Fig. 7.

In the next example solution a fully constrained concrete specimen modeled by four 4-node plane stress elements is subjected to a uniform temperature loading ${}^{t}\theta$. The initial temperature is zero degrees and the temperature is raised to 450°C leading to material crushing, see Fig. 9. Note the increase in the crushing strength of the material is due to the biaxial stress conditions.

Next, in Fig. 10, a simple plane stress concrete element subjected to biaxial compression loading is considered. After crushing, the material relation of Sec. 2.4 is used, i.e. all Young's moduli are set to $\tilde{E}_{p3}$.

In a further example solution, a single 2D plane stress element is loaded to trace the post-cracking behavior of the concrete material model under biaxial loading in comparison with uniaxial loading (see Fig. 11). The shift in the stress–strain 1D response depends on the σ_{p1}, σ_{p2} relation (positive/positive, positive/negative) as well as on the magnitude of the Poisson ratio. It should be noted that strain-softening post-cracking models ($\xi > 1.0$) are to be used with caution since such models may lead to a nonunique solution [14] (see also Sec. 3.2).

Extensive cracking and complex post-cracking behavior can be observed in the analysis of concrete pressure vessels. In this part of the paper we present detailed solutions of two 'reduced' models. Analyses of the complete pressure vessel structures are presented in Part II of the paper.

Figure 12 shows a simple finite element model of a part of the Sandia pressure vessel. This model represents a slice of the vessel at the elevation 5.969 m. The slice is subjected to boundary and loading conditions corresponding to the whole structural behavior when the vessel is under internal pressure. Three eight-node axisymmetric elements were used to model the concrete of the pressure vessel. The 1-node axisymmetric and 2-node truss elements were used to model the steel reinforcements. Figure 13 shows crack distributions for different load levels. In Fig. 14 a comparison with experimental data is presented. Note that in Fig. 13 cracks are plotted at the integration points, the size of a cracking symbol depends on the con-

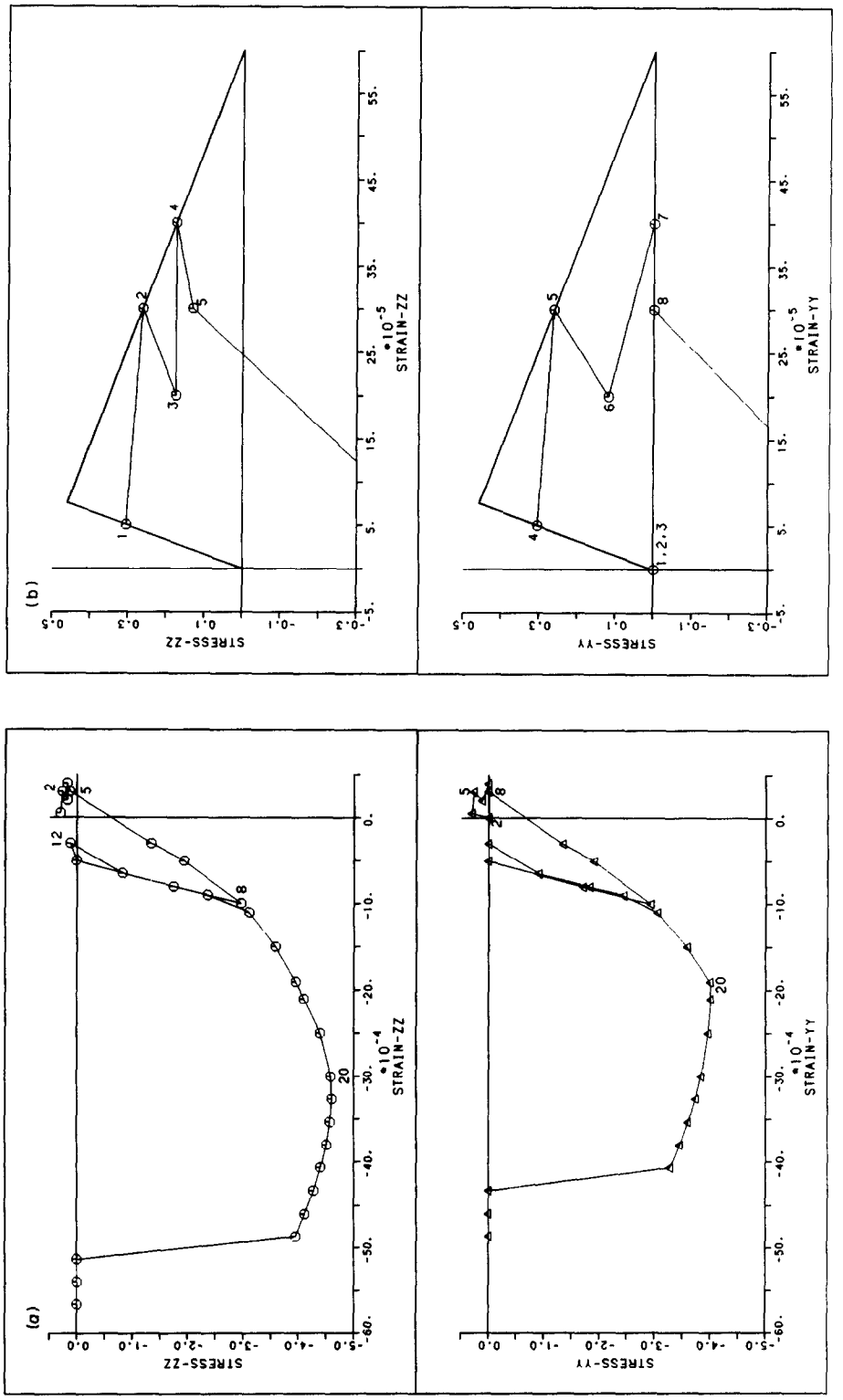

Fig. 7. Response of model subjected to biaxial strain loading. $\tilde{E}_0 = 6100$ ksi, $\nu = 0$, $\tilde{\sigma}_c = -3.74$ ksi, $\tilde{e}_c = -0.002$, $\tilde{\sigma}_u = -3.225$ ksi, $\tilde{e}_u = -0.003$, $\tilde{\sigma}_t = 0.458$, $\xi = 8.0$, $C_1 = 1.4$, $C_2 = -0.4$. (a) Stress–strain response. The numbers indicate solution load steps. For detail in tensile region, see (b). (b) Stress–strain response in tensile region. Note the decrease in tensile strength in the y direction for step 7 due to the compressive stress in the z direction.

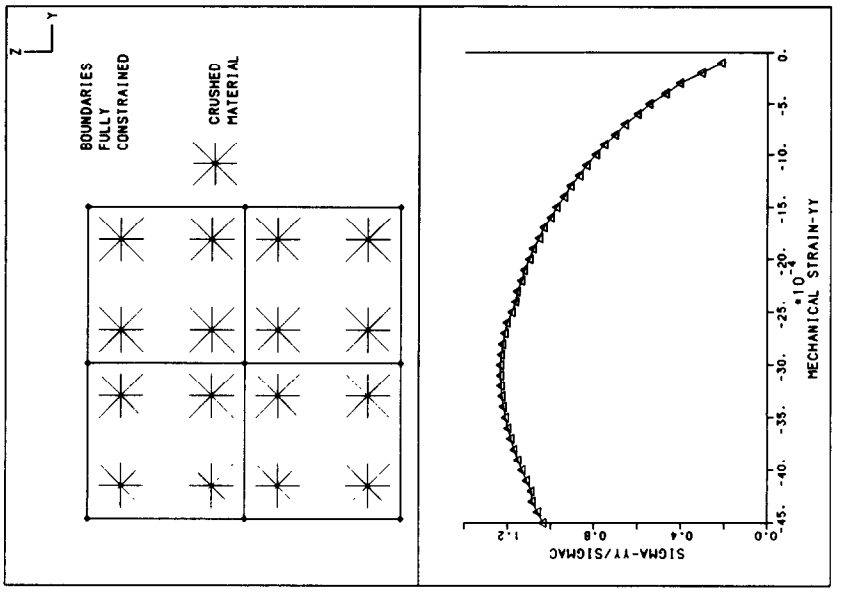

Fig. 9. Thermal loading on a specimen fixed on boundaries. Top: crushed material reached at mechanical strain $e_{yy} = e_{zz} = -30 \cdot 10^{-4}$. The size of the crushing symbol depends on the contributing volume at the integration point. Bottom: stress–mechanical strain relation as calculated by ADINA.

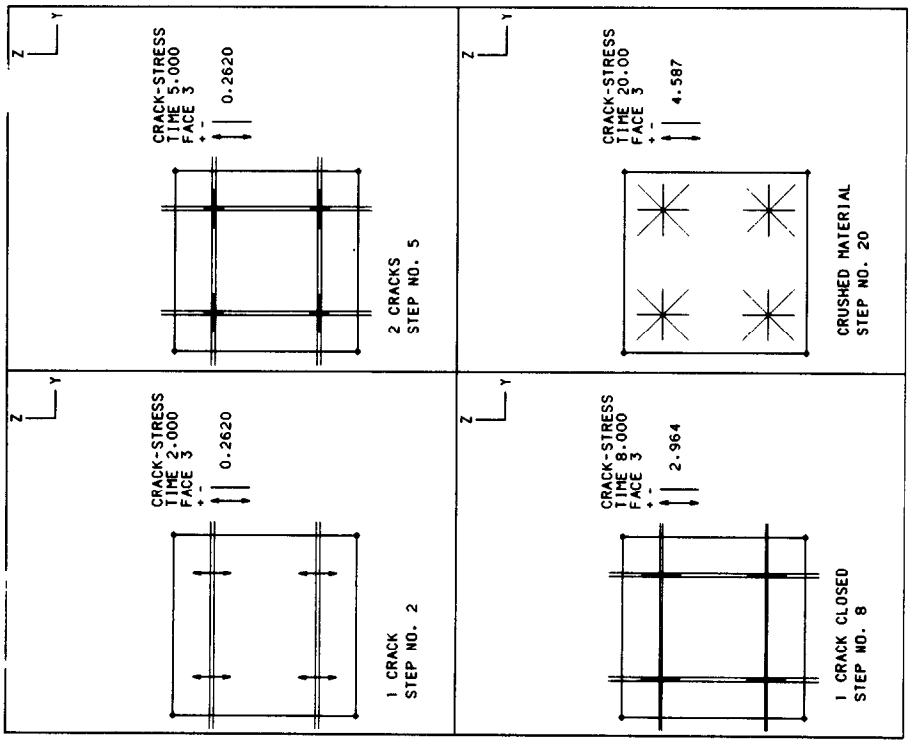

Fig. 8. Material failure for different load steps indicated in Fig. 7. The parallel lines indicate cracks. At step 8, the horizontal cracks are closed which is indicated by the smaller distance between the horizontal lines. Crushing is indicated by the star symbol.

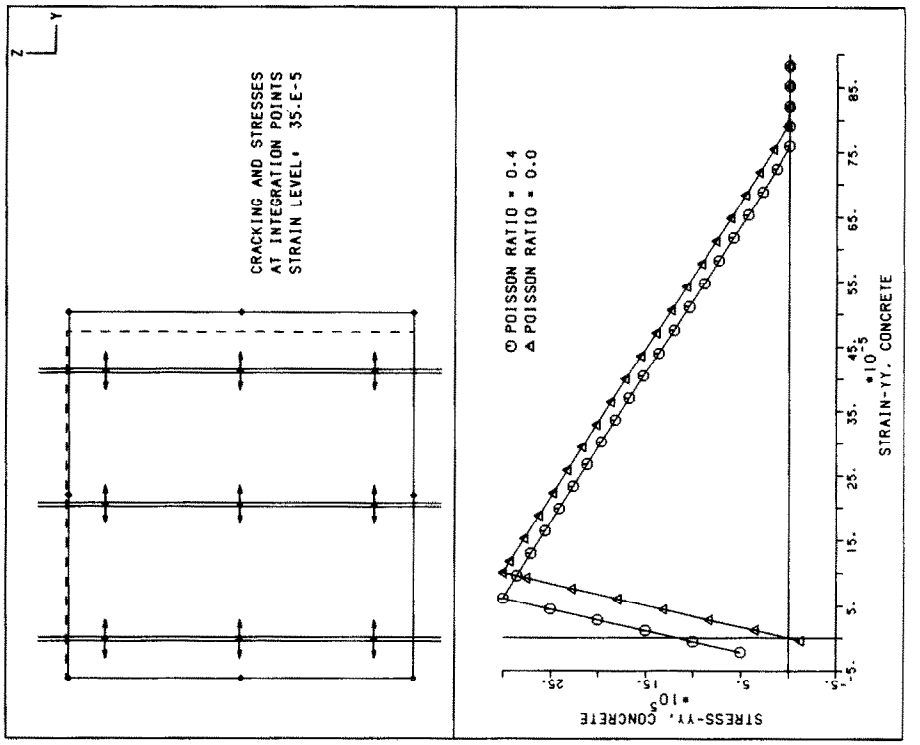

Fig. 11. Biaxial tension of a specimen. Top: state of stress and cracks at $e_{yy} = 0.00035$, case $\nu = 0.4$. Bottom: stress–strain response calculated by ADINA.

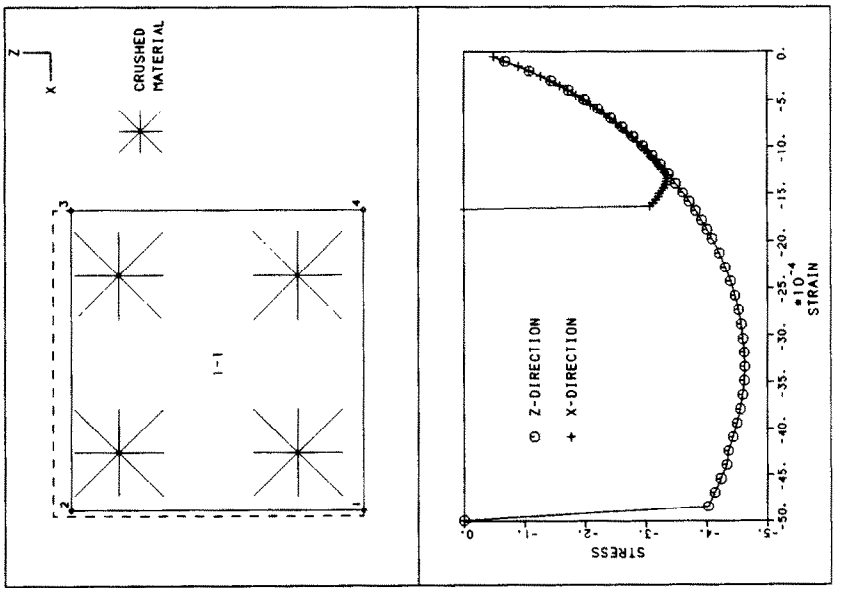

Fig. 10. Biaxial compression of a specimen. Top: crushed material at strain level $e_{zz} = -0.0034$. Bottom: stress–strain response as calculated by ADINA.

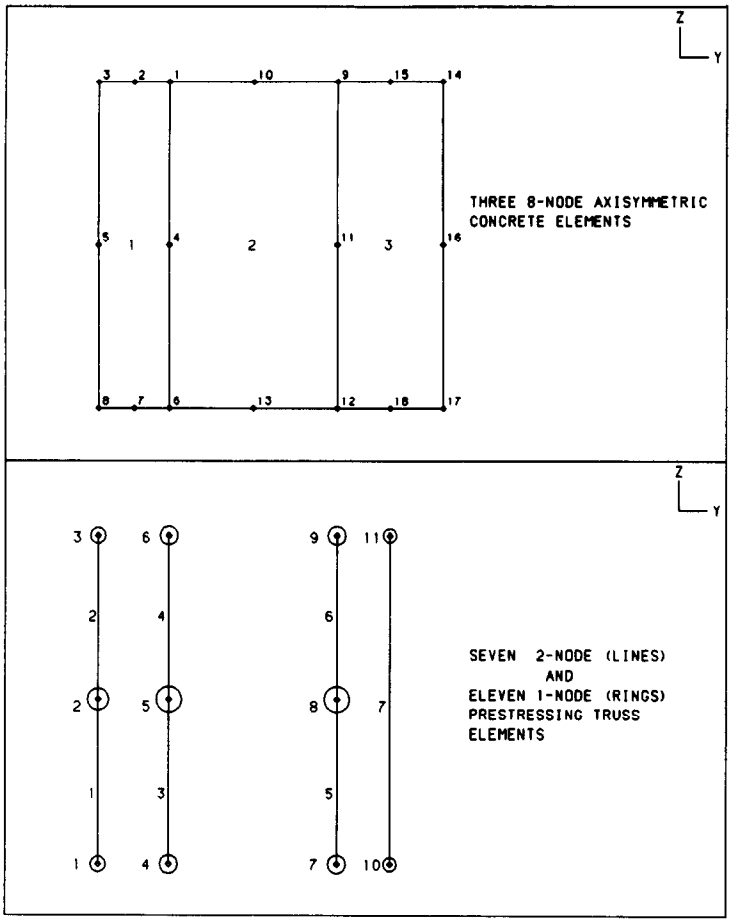

Fig. 12. A finite element model for a slice of the Sandia pressure vessel at elevation 5.969 m (see also Fig. 19). Top: 2D axisymmetric concrete elements. Bottom: prestressing truss elements.

tributing volume at the integration point, circles represent hoop cracks and two parallel lines a short distance apart represent cracks in the Y–Z plane. A smaller distance between the parallel lines is used when the crack is closed.

A simple model of a part of the PWR pressure vessel (this vessel is also considered in Part II of the paper, see Fig. 30) is shown in Fig. 15. As for the Sandia vessel, a slice of the PWR vessel is considered. This slice now corresponds to the height 22.30 m. Two 8-node axisymmetric finite elements were used to model the concrete of the vessel. The steel hoop, longitudinal and radial reinforcement is modeled using 1-node axisymmetric and 2-node truss elements. The model is subjected to boundary and loading conditions that correspond to the response of the complete structure. The crack distributions for different solution times are shown in Fig. 16. Note that three cracks have been formed at some of the integration points at the final load level. In Fig. 17 the solution results are compared with the results of an analysis using a simple force-balancing method.

2.8. *Concluding remarks*

The objective of Part I of this paper was to summarize the current status of our concrete material model. The model can be employed in a number of important concrete analyses, notably for collapse analyses of two- and three-dimensional concrete structures. One important aspect is the generality of the model with respect to the stress–strain law and failure surfaces used. Also, the model is deemed computationally efficient because relatively large incremental load steps can be employed (see Figs 14 and 17).

Although a powerful model already, further improvements to the concrete model are surely desirable. Some features that would appropriately gain further research attention are the modeling of time-dependent behavior, a more accurate representation of the post-crushing response and further refinements in modeling the tensile-stiffening behavior, the effects of Poisson's ratio and cyclic loading conditions.

3. PART II: APPLICATIONS OF ADINA 5.0 TO THREE TEST STRUCTURES

Taylor Woodrow plc (TW), a worldwide engineering group, has been involved in the design and construction of nuclear power structures for over 30 years. During this period much knowledge has been gained on the short- and long-term behavior of

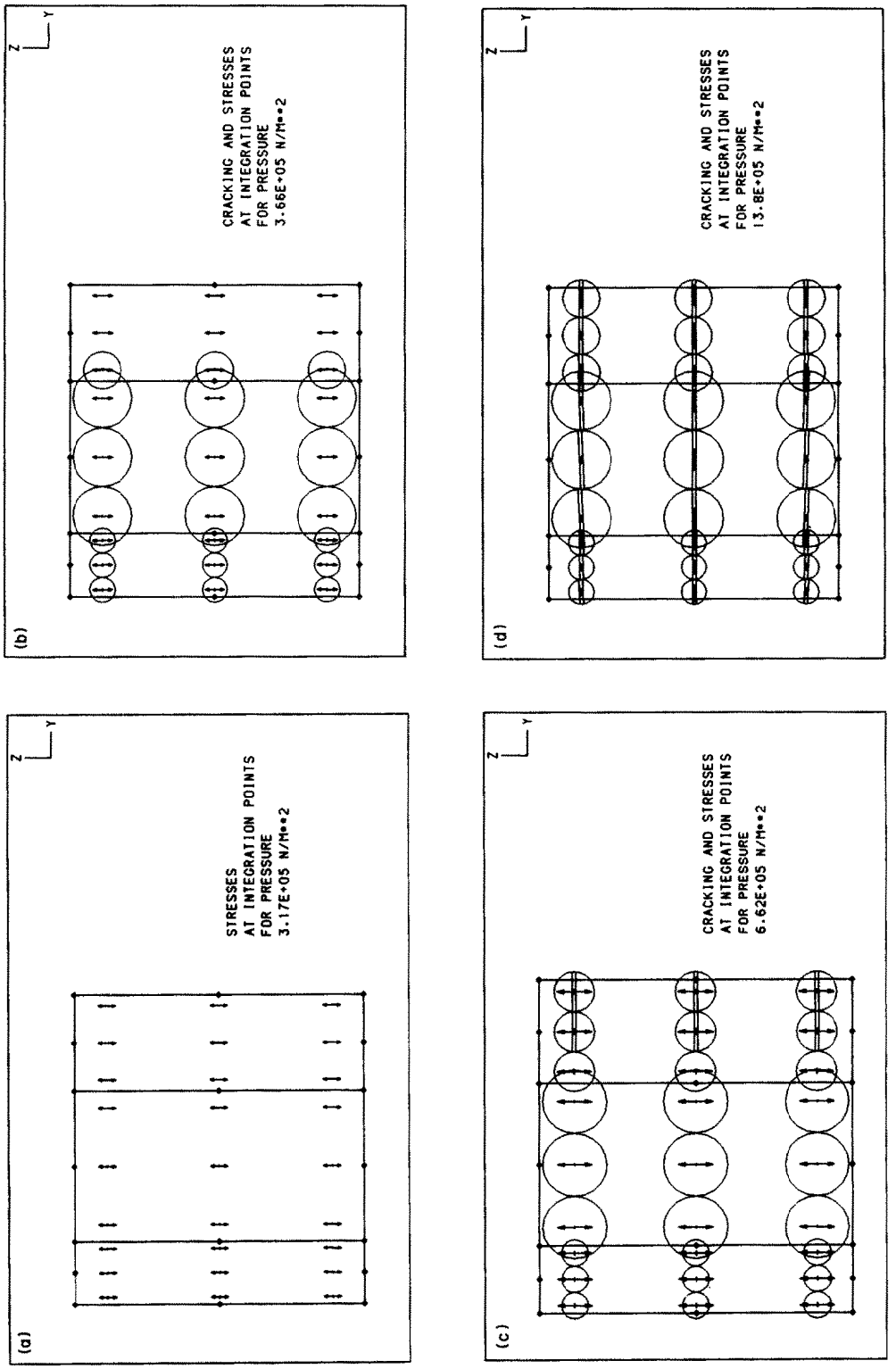

Fig. 13. Development of cracks in the Sandia model of Fig. 12. In 3D analysis a crack at an integration point is represented by two disks a small distance apart, the crack lying in the plane between the disks. Hence, in this figure parallel lines represent cracks in the Y–Z plane; circles represent hoop cracks. The size of the two disks corresponds to the contributing volume at the integration point.

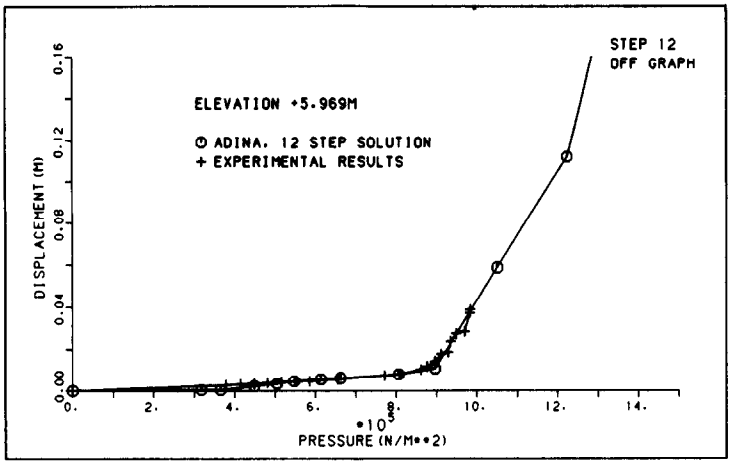

Fig. 14. Displacement–pressure response of the Sandia pressure vessel.

concrete and a comprehensive degree of expertise has been accumulated in the design, analysis and testing of a wide range of concrete structures. TW has extensive in-house testing facilities which at first were used in support of the nuclear industry and later have been involved in a wider range of concrete structures including the offshore, civil and conventional building areas. This test work has supplemented the analytical work which itself has augmented the testing.

To increase its analytical capabilities it was decided to acquire a nonlinear finite element system which included a concrete material model. After reviewing a number of alternatives TW obtained the ADINA 81 code in 1983. In using the package on a wide range of reinforced concrete structures a number of potential improvements to the concrete model could be envisaged, and TW decided to add in extra features and change existing ones (see [10, 15]). The form of these changes and their influence were shared with ADINA R & D, Inc. and have been incorporated within some of the improvements to the concrete material model that are found in the latest ADINA 5.0 code.

The work presented in this section was originally carried out using the modified ADINA 81 system but has subsequently been rerun using the latest ADINA 5.0 version, these later results being presented now. Three applications are given of which two represent situations where the original analysis was carried out prior to the test results being available. The third analysis supplemented the design but will eventually be used in conjunction with a physical model at present under construction in the Taylor Woodrow Laboratories.

3.1. *One-sixth scale model of a reinforced concrete containment*

The U.S. Nuclear Regulatory Commission (NRC) has initiated the construction and testing of a series of scale models of containment buildings. This formed part of a containment integrity program, one

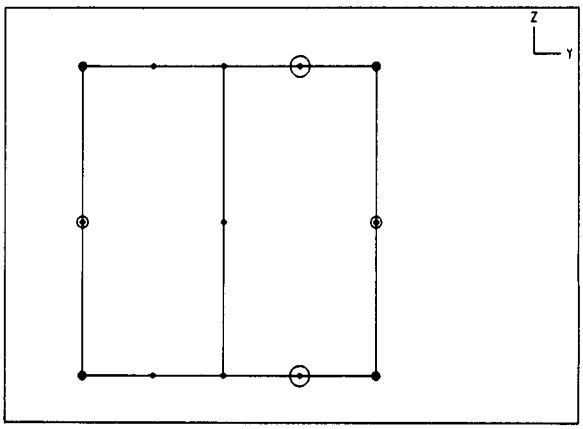

Fig. 15. A finite element model for a slice of the PWR pressure vessel at elevation 22.30 m (see also Fig. 32).

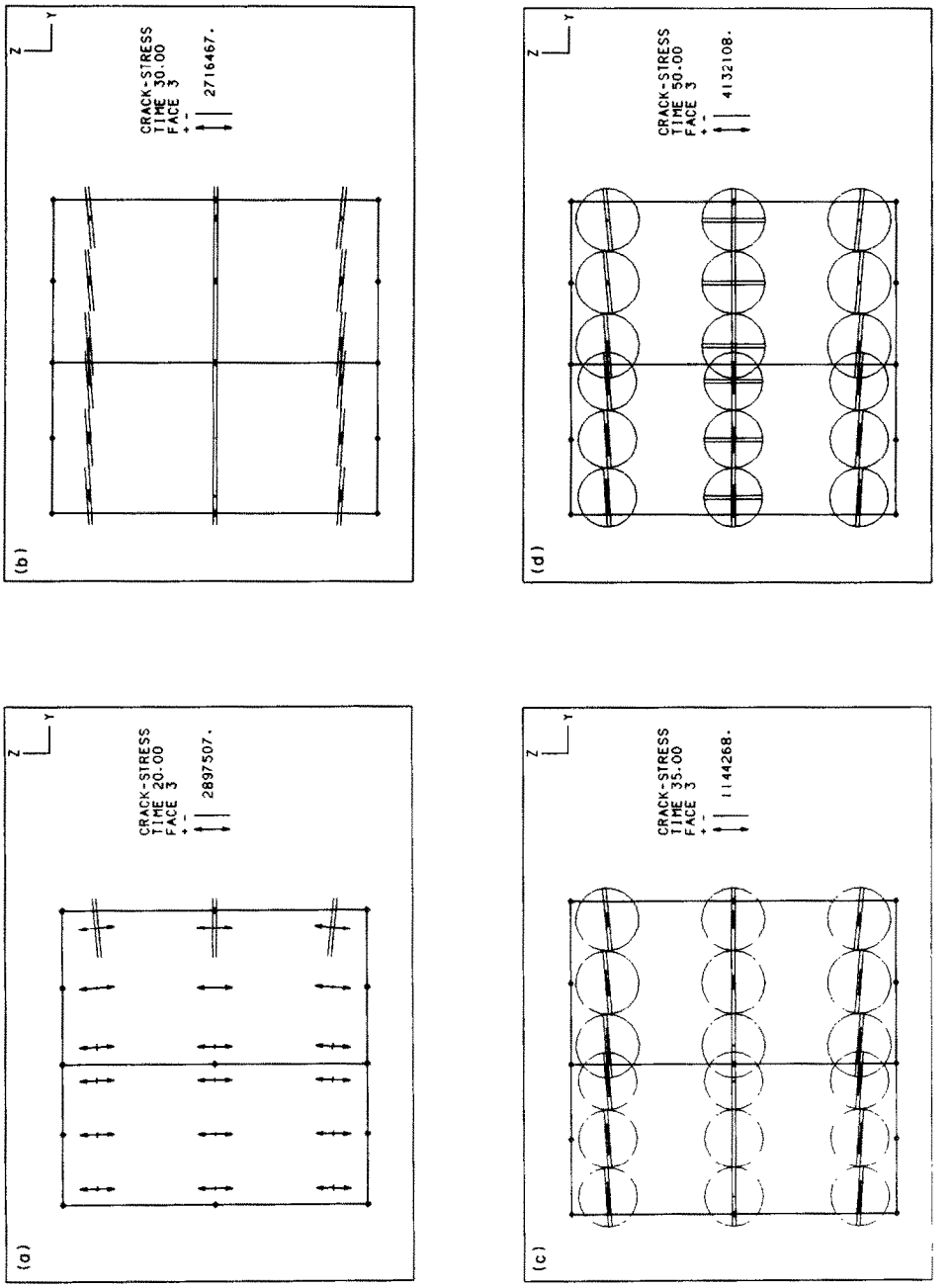

Fig. 16. Crack distributions in the model of Fig. 15: (a) at pressure/design pressure = 1.0; (b) at pressure/design pressure = 1.6; (c) at pressure/design pressure = 2.0; (d) at the final applied load step, pressure/design pressure = 2.2.

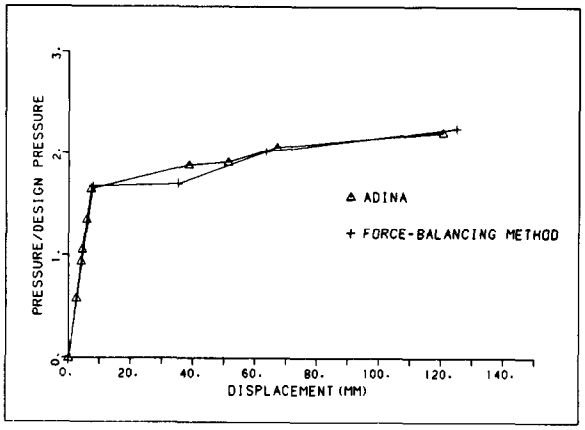

Fig. 17. Load–displacement response for the PWR model of Fig. 15.

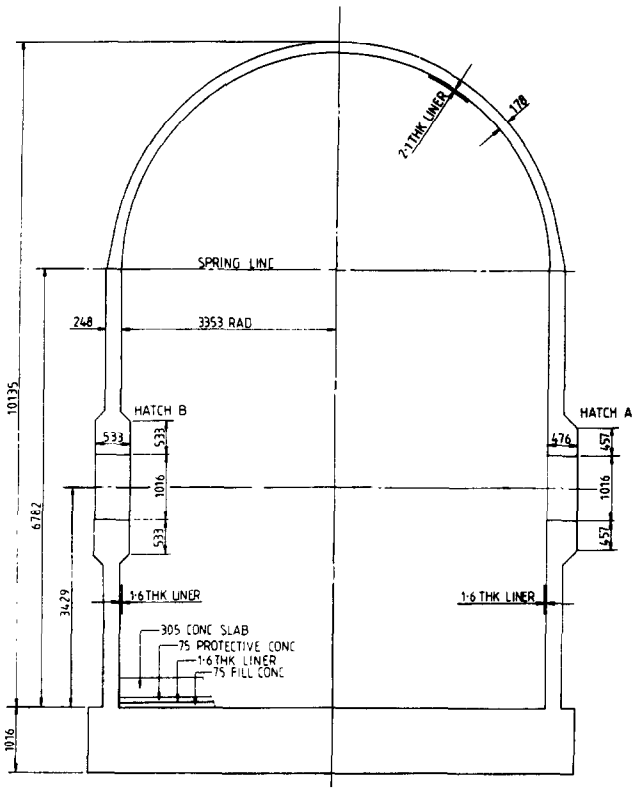

Fig. 18. General arrangement of the Sandia pressure vessel. It is a 1/6th scale model.

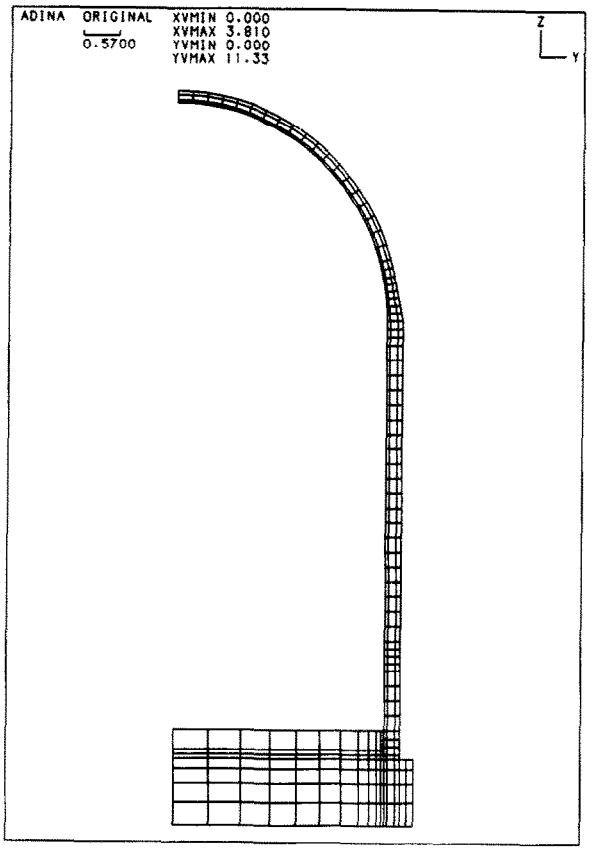

Fig. 19. Finite element mesh of the Sandia pressure vessel.

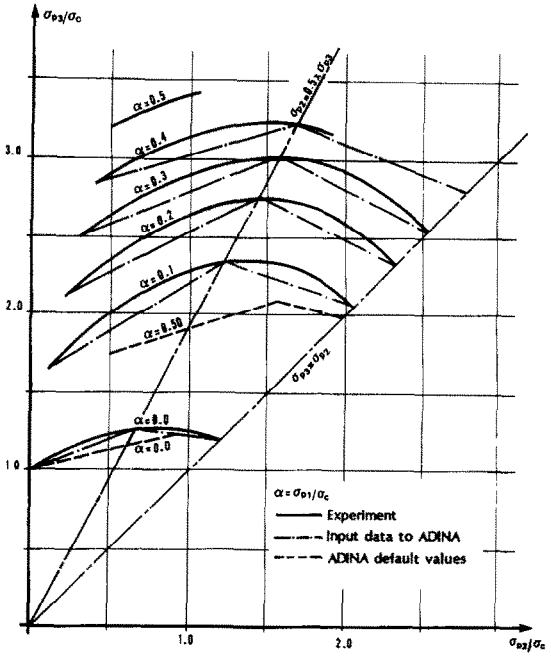

Fig. 20. Compressive failure envelope used for analysis of the Sandia pressure vessel. Comparison of experimental values, ADINA input values used in the analysis and ADINA default values.

item of which was the construction of a one-sixth scale model of a reinforced concrete containment. This structure was to be analyzed prior to testing by a number of participating organizations, four from the U.S. and six from Europe. One of the groups submitting an analysis was sponsored by the Central Electricity Generating Board (CEGB) of the United Kingdom. Work was carried out for the CEGB by the Nuclear Design Associates (NDA), a joint venture of Taylor Woodrow and Sir Robert McAlpine.

The analysis formed part of a 'Round Robin' pretest series of analyses, these being documented in a NRC document [16] and formed part of the NDA validation work for the use of the ADINA code [17]. Details of the test structure are shown in Fig. 18. It can be seen that whilst in general being an axisymmetric structure, some degree of divergence from this occurs at major penetrations, and with the disposition of reinforcement. The ADINA analysis carried out was assumed to be axisymmetric, the local three-dimensional effects being investigated by separate linear analyses.

The finite element mesh produced for the ADINA analysis is shown in Fig. 19. The concrete properties used in the analysis were as follows,

initial E value $(\tilde{E}_0) = 24{,}800$ MN/m^2
crushing stress limit $(\tilde{\sigma}_c) = -41$ MN/m^2
crushing strain $(\tilde{e}_c) = -0.00186$
ultimate stress $(\tilde{\sigma}_u) = -30$ MN/m^2
ultimate strain $(\tilde{e}_u) = -0.0032$
tensile limit $(\tilde{\sigma}_t) = 4.1$ MN/m^2
Poisson's ratio $(v) = 0.2$.

Compressive failure envelopes were based on published results [18], these being shown in Fig. 20 in order to indicate how they deviate from the ADINA default values. In general TW has used these failure curves for most analyses as it is felt they fit a wider range of test results than the default values, although the deviation is only of concern in the higher triaxial stress states. As an aside, it is TW's policy when using ADINA to try to have a standard approach wherever possible, therefore when dealing with conventional reinforced concrete most input parameters are unchanged from one analysis to the next apart from the compressive limit. This even covers the choice of tensile limit where, unless otherwise directed by circumstances or direct evidence, the value is assumed to be 10% of the compressive limit.

The reinforcement was treated as a multilinear elastic model. The main vertical and hoop reinforcement could be modeled easily but towards the bottom of the wall there existed diagonal seismic reinforcement. It was considered sufficiently accurate to model this as an equivalent extra set of vertical and hoop bars. Orthogonal bars in the base were likewise replaced by equivalent replacement hoop and radial bars.

The physical model contained a steel liner. ADINA does not as yet contain an axisymmetric shell element, therefore the liner was modeled using hoop and meridional truss elements with due allowance for the Poisson's ratio effect that would be in the plate but which is missing in the equivalent set of truss elements.

Finally the soil was modeled as a set of spring elements. Due to the relatively large thickness of the bottom cap the choice of spring stiffnesses was not expected to significantly influence the final ultimate load.

The model was constructed by Sandia National Laboratories and tested in July 1987, by which time all analysis work had been carried out, supplied to the NRC and disseminated in a report of May 1987 [16]. The test consisted basically of an initial low pressure cycle up to 1.15 times design pressure. With design pressure at 0.317 MN/m^2 this represents an initial loading of 0.365 MN/m^2. After returning to zero pressure a high pressure test was performed up to the ultimate pressure sustainable by the structure. In the analysis the initial cycle was not included, the loading consisting of a gradual application of pressure until failure was indicated.

The following commentary will help to describe both the ADINA analysis findings and the complex behavior predicted.

0.138 MN/m^2—Cracking occurs at the wall base junction due to bending. This represents less than 44% of design pressure, but subsequent cracking in this area progresses across the section in a controlled manner. The outcome is that a 'plastic' hinge forms here.

0.345 MN/m^2—Vertical cracking (that is cracks due to hoop stresses) commence at the mid-height and quickly spread to reach the dome spring line at 0.365 MN/m^2.

0.400 MN/m^2—Horizontal cracking (due to bending and axial tension) appears on the outside face of the wall and quickly spreads through the thickness and along the wall towards the dome and wall base junction. By about 0.55 MN/m^2 the dome and wall are almost completely cracked through, the pressure being resisted by the liner and reinforcement.

0.552 MN/m^2—Cracking occurs at the middle of the underside of the bottom cap. By 0.855 MN/m^2 these cracks have extended across the entire underside.

0.565 MN/m^2—Initial yield of the liner at mid-height in hoop direction, again rapidly extending up and down the structure.

0.855 MN/m^2—Inside hoop reinforcement at mid-height reaches first yield.

0.890 MN/m^2—All layers of hoop reinforcement at mid-height have yielded resulting in rapid expansion of the wall.

1.000 MN/m^2—By this pressure most reinforcement has yielded.

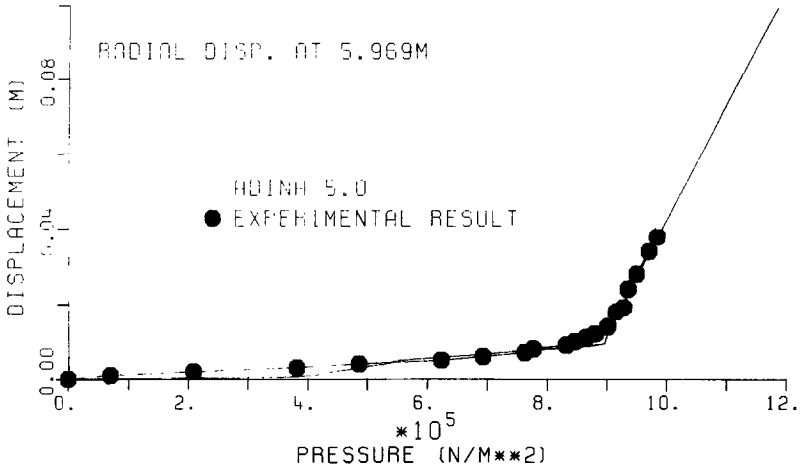

Fig. 21. Analysis and experimental displacement response at the mid-height of the radial movement.

1.100 MN/m²—Crushing of outer wall at wall-base junction followed by complete failure at this location.

It should be pointed out that in most work to date TW has preferred not to use iterations but to progress the load at a controlled and sufficiently slow rate with holds of pressure at chosen pressure levels. This, particularly with our earlier work, seemed to allow the analysis to progress further but care was necessary especially at points of rapid change and near ultimate.

A few figures have been produced to illustrate the behavior of the containment. Figure 21 shows the comparison between analysis and experiment of the mid-height radial movement. This is the dominant movement in the structure and so a good choice for comparison purposes. As can be seen the actual test reached 1.0 MN/m² at which stage excessive leakage occurred, probably through a large liner tear near to a major penetration. The correlation between the two curves is very high, especially as the small deviation over the range 0–0.4 MN/m² can be accounted for by the initial low pressure test carried out. Reference to the table of events indicates that much cracking could have occurred, therefore on repressurization these regions would have zero tensile strength.

Two other plots (Figs 22 and 23) show global views of the displaced shape and the extent of cracking. Figure 22 shows global views of the displaced shape at various pressure levels, all displacements being drawn to the same scale. Figure 23 shows the extent of cracking at various pressure levels.

3.2. *Alkali–silica reacted beam*

During the period 1984–1989 the Road Directorate of Denmark initiated a project to study the load carrying capacity of structural members subjected to alkali–silica reaction (ASR). One item of this involved studying the shear strength of concrete beams subject to ASR.

At a conference in Denmark in 1988, attendees were invited to predict the failure load of one of the beams that had been tested, but for which the results had not yet been disclosed. The results of this test were revealed in a subsequent report [19] together with photographs of crack patterns on similar tested beams.

The analysis was carried out on the test beam shown in Fig. 24. The beam deviates from a conventional test by virtue of the ASR, and from the lack of shear reinforcement in the zone of maximum shear. The mesh used is shown in Fig. 25. The relevant properties chosen for the concrete were based on cores removed from the beam. Both vertical and horizontal cores were taken, the former being 40% stronger. Being unable to incorporate this non-isotropic behavior a mean compressive strength of 33.0 MN/m² was used together with a tensile strength of 3.3 MN/m².

The analysis reached an ultimate load of 132 kN at each load position. In the experiment the specimen first failed with a shear failure on one side at 127.4 kN.

Figure 26 shows the load–deflection curve at mid-span and it can be seen that the final failure was fairly abrupt even though a great deal of cracking had occurred in both the flexure and shear zones. This could be interpreted as basically indicating a shear failure. Figure 27 shows the extent of cracking at various load levels whilst Fig. 28, which plots the largest strains, gives a clear picture of the gradual flexural damage, initiating on the mid-section bottom face very early on, and progressing slowly through the depth and outwards towards the supports. The subsequent shear damage is seen to be quite sudden. Comparisons with a similar beam can be made in Fig. 29 which shows the same form of progressive damage with a rapid change on the left hand side at ultimate load.

On studying the Danish report it was seen that the

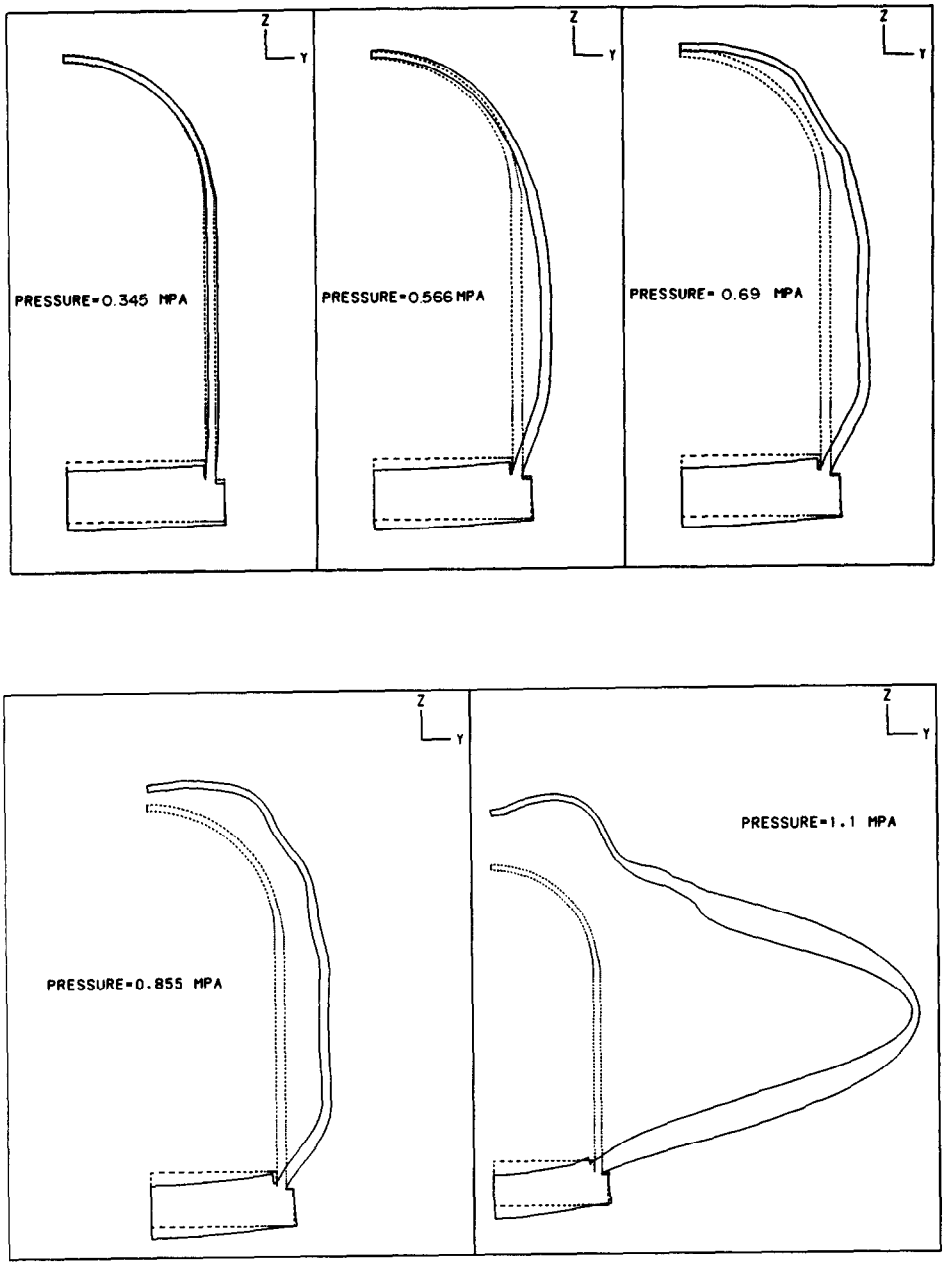

Fig. 22. Global view of the displaced shapes of the Sandia pressure vessel. Displacements magnified by a factor of 167.

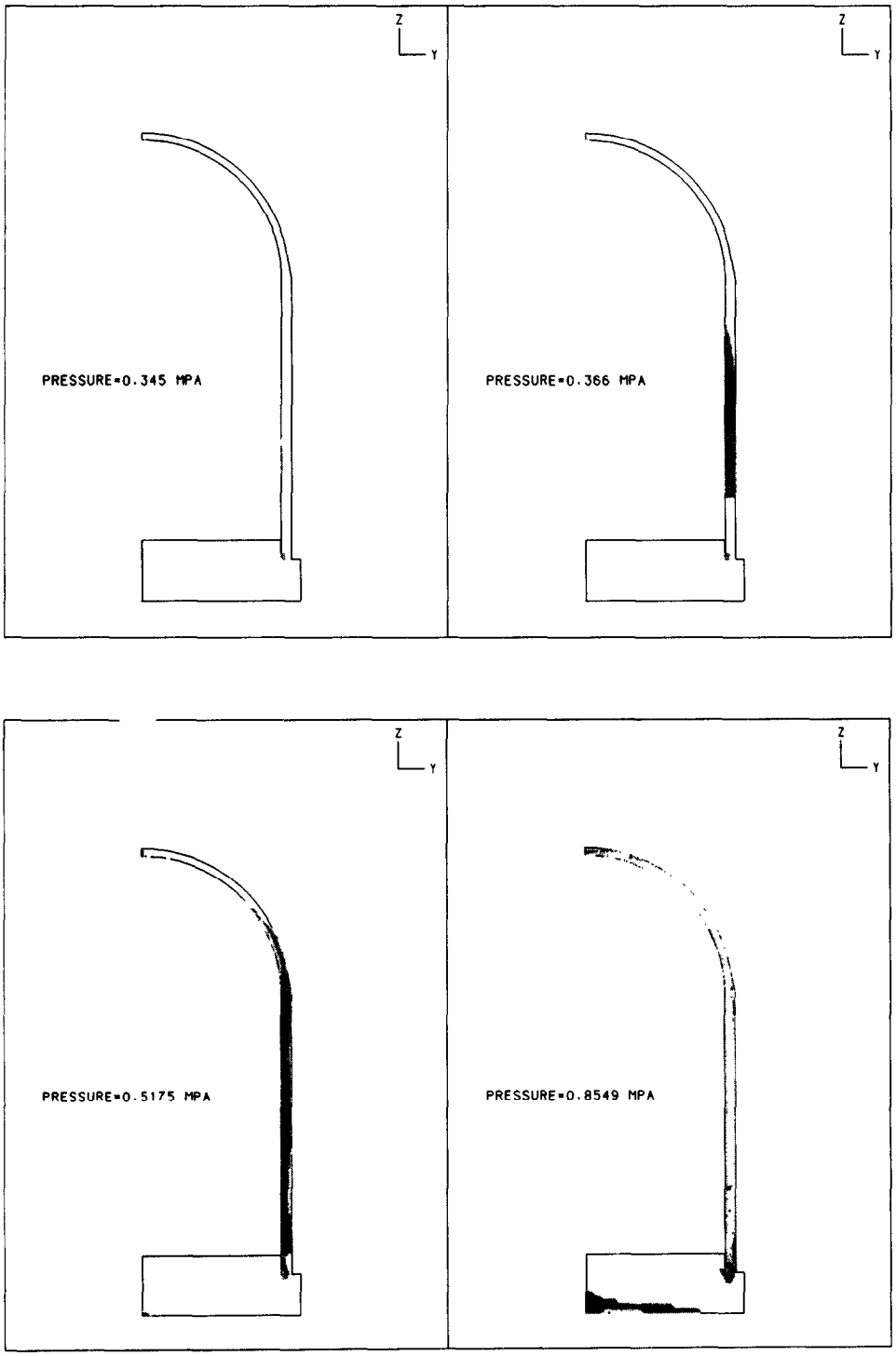

Fig. 23. Global view of the extent of cracking in the Sandia model. In the original, yellow—1 crack, blue—2 cracks, red—3 cracks.

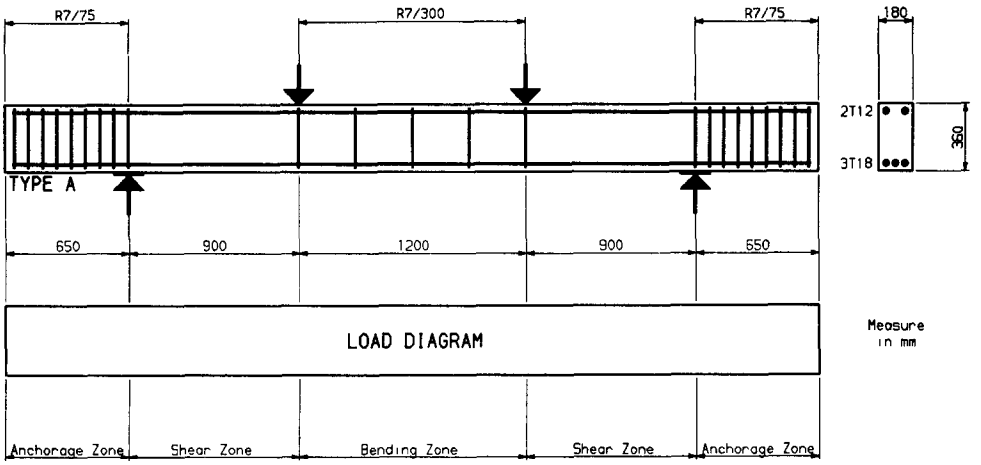

Fig. 24. Alkali–silica reacted beam. Geometry, reinforcement and load diagram.

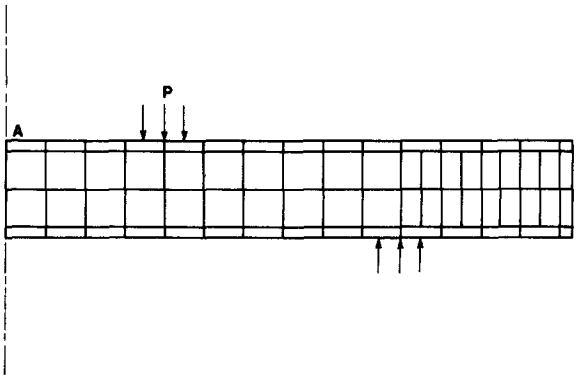

Fig. 25. Finite element model, 8-node plane stress elements for the beam of Fig. 24.

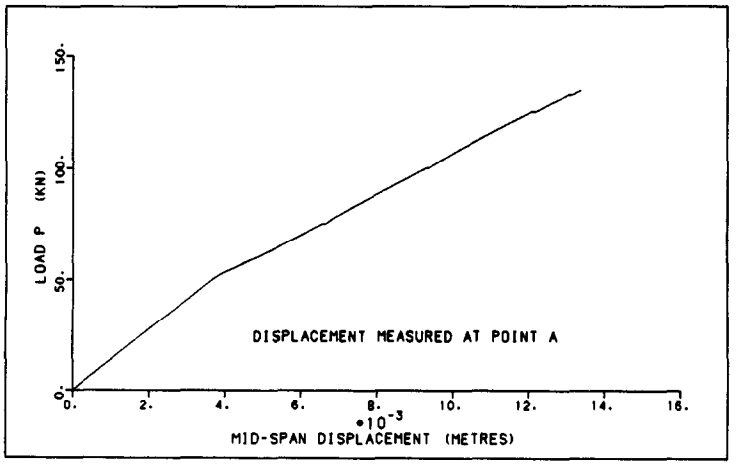

Fig. 26. Load–displacement response as predicted by ADINA for the alkali–silica reacted beam.

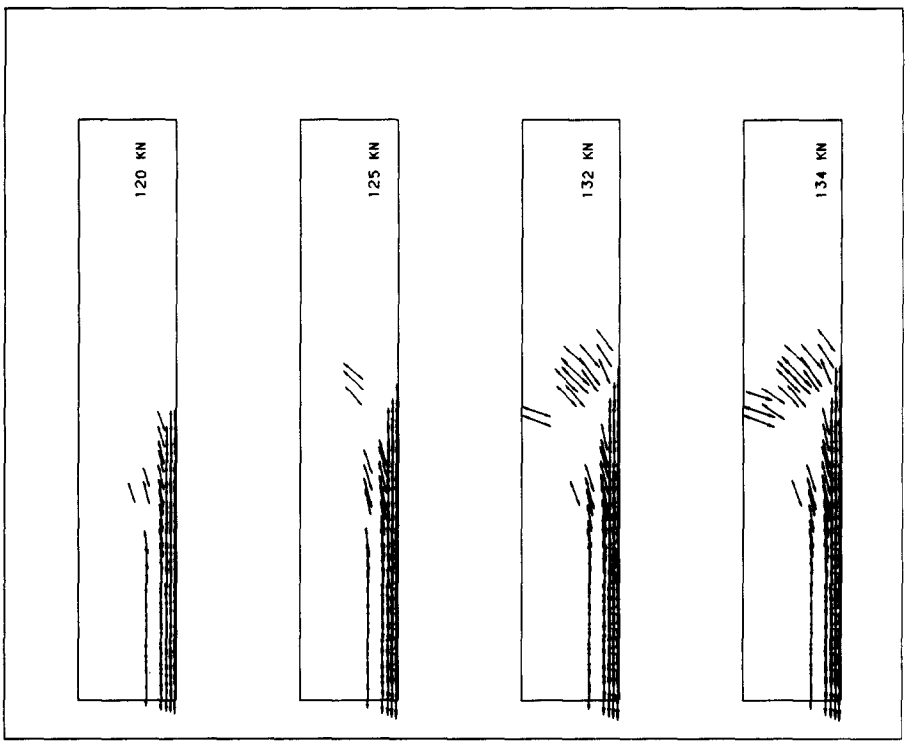

Fig. 28. The maximum principal strain distributions at various load levels for the alkali–silica reacted beam.

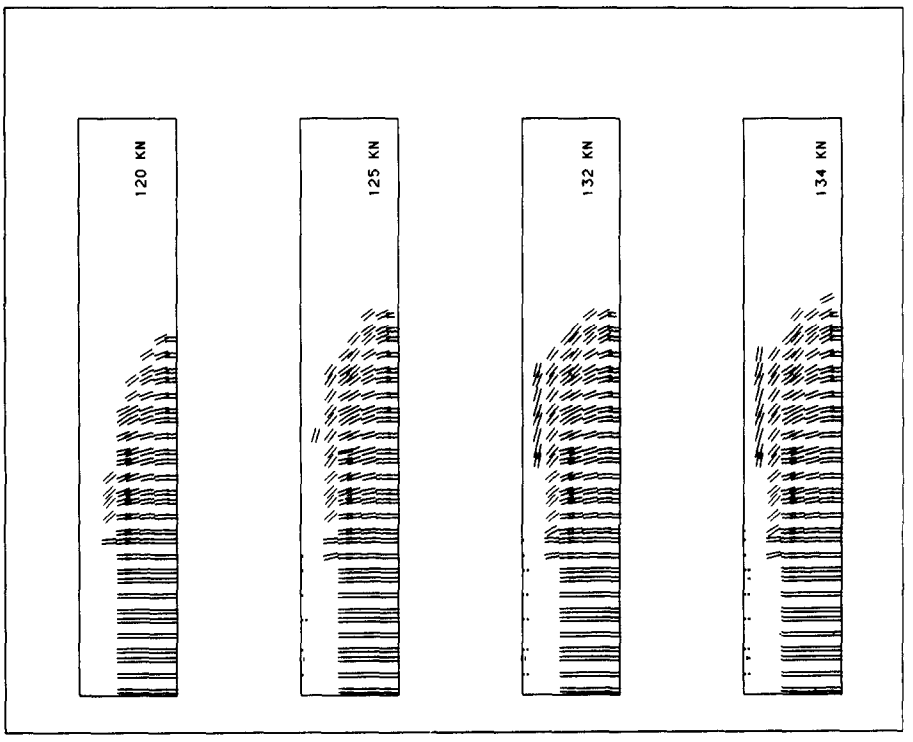

Fig. 27. Extent of cracking at various load levels for the alkali–silica reacted beam.

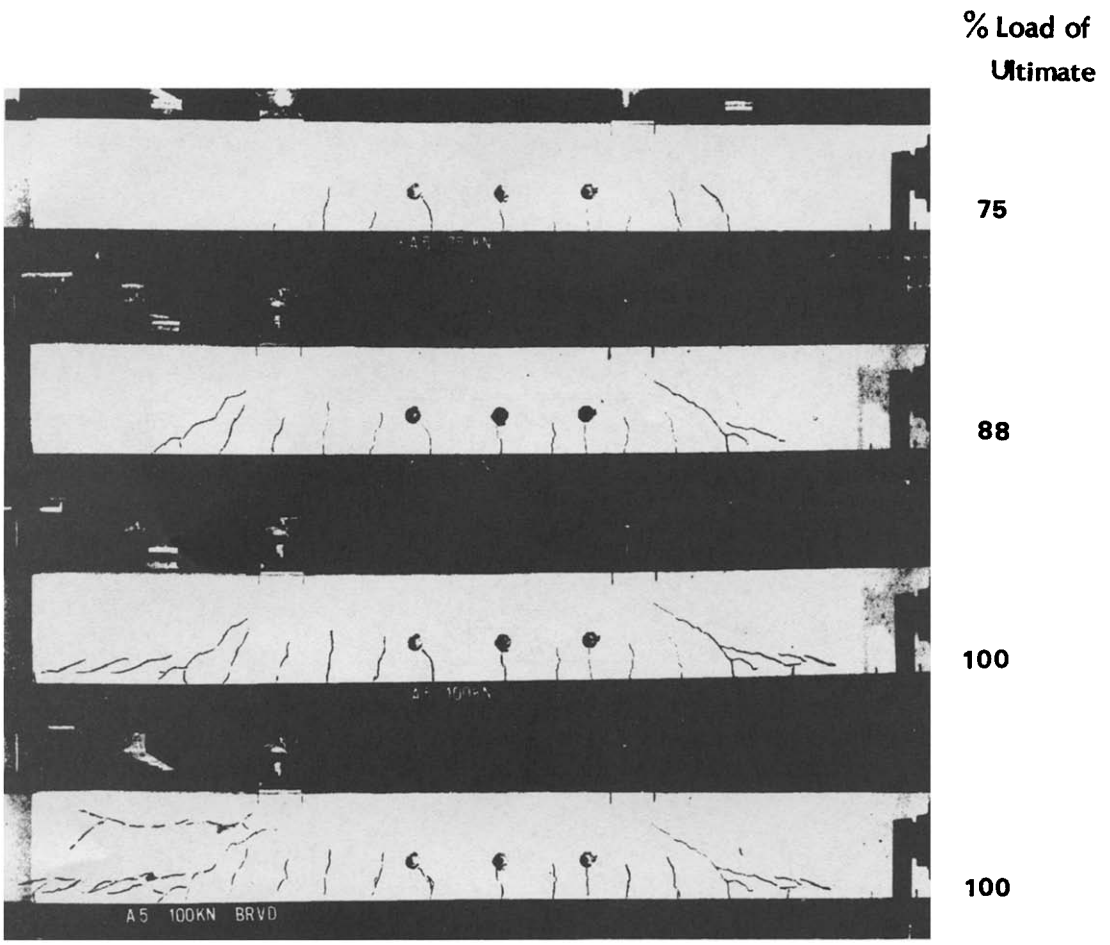

Fig. 29. Experimental results of developments of cracks during loading of an alkali–silica reacted beam.

ASR beams were judged against unaffected specimens. On testing these it was found that very early shear failure initiated in the shear zone resulted in lower strengths even though the unaffected concrete had a higher strength. It was judged that the ASR caused a great deal of micro-cracking of the concrete making the beam more ductile, hence redistributing the stresses more efficiently in the shear zone.

To investigate this it was decided to rerun the analysis with a higher concrete strength of 58.2 MN/m^2, this being the quoted cylinder strength of the undamaged concrete. Just making this change resulted, as expected, in an increase in ultimate load, contrary to the test results. On reflection, the shear zone is basically unreinforced concrete, therefore cracking should be concentrated in fewer cracks and should propagate more rapidly. This is very similar to the situation of no tensile stiffening after failure and a reduced shear reduction factor and hence a run was made to use a tensile stiffening factor of 1.2 instead of 8 and a shear reduction factor of 0.01 instead of 0.5. Whilst the problem showed much more distress in the shear zone it reached higher than expected loads.

Study of the crack dispositions and strains still indicates a smearing of cracks instead of the expected dominant single crack. Whilst of not too much significance in conventionally reinforced structures, this phenomenon could be more important in analyzing problems involving mass concrete.

3.3. *Sizewell 'B' PWR prestressed concrete containment*

The main difference between this containment and the Sandia test structure is that the Sizewell structure is prestressed by longitudinal, radial and hoop tendons. Nonlinear analyses have been applied to the full scale structure now under construction at Sizewell, United Kingdom and to a tenth scale model which, at the time of writing, is under construction at the Taylor Woodrow Laboratories.

Figure 30 shows the form of the structure which is in essence axisymmetric except for the major wall penetration (not indicated on this diagram), the tunnel in the base and the disposition of prestress. The latter is provided by hoop tendons that cover overlapping 240° segments of the wall and the lower

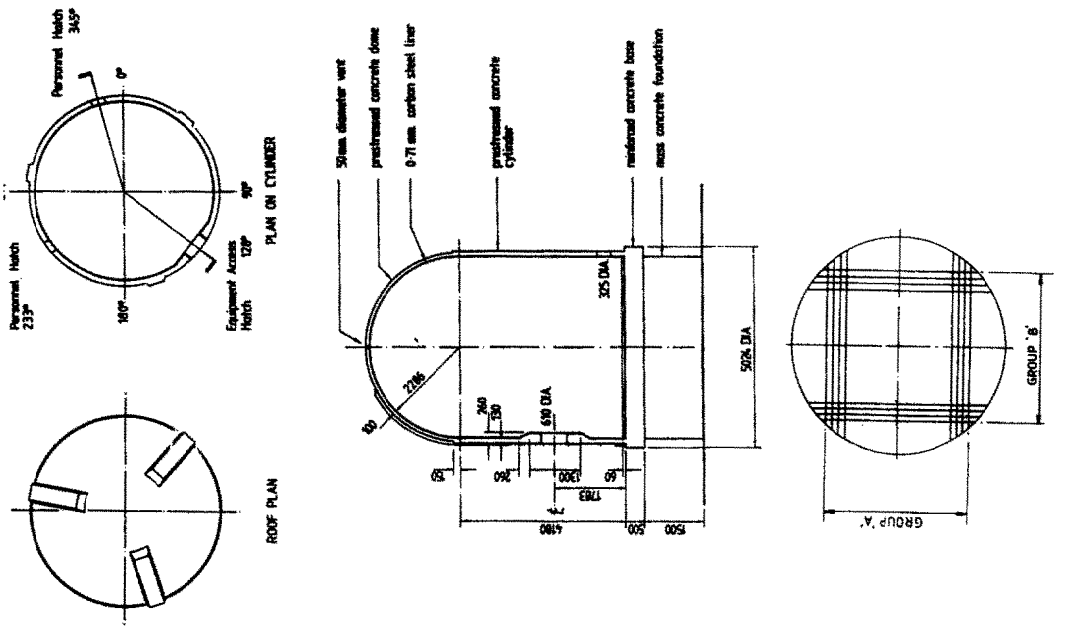

Fig. 31. PWR containment, tenth scale model: some structural details.

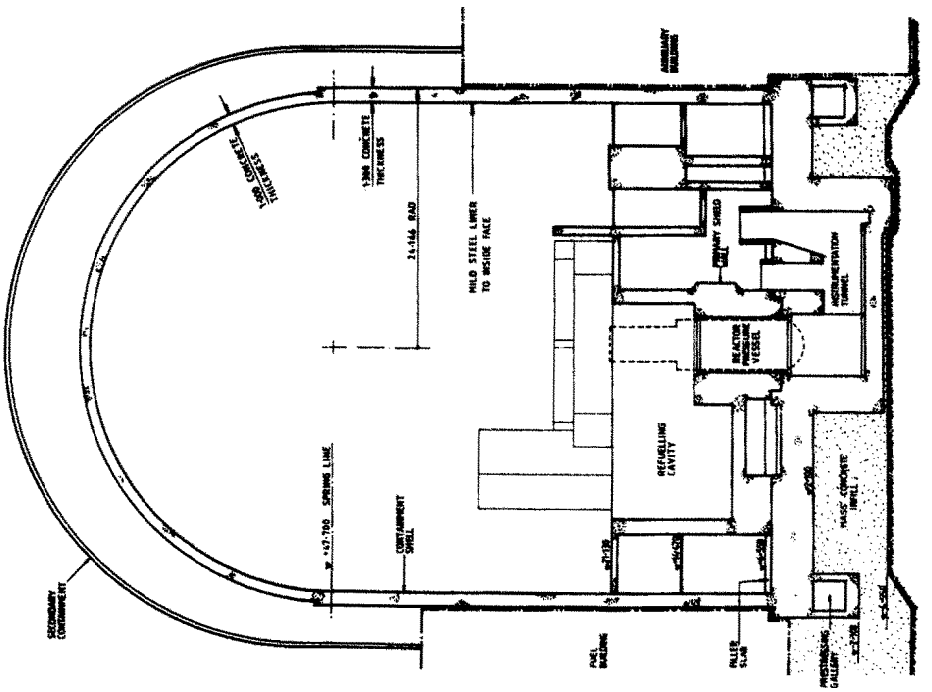

Fig. 30. PWR prestressed concrete containment section through reactor building.

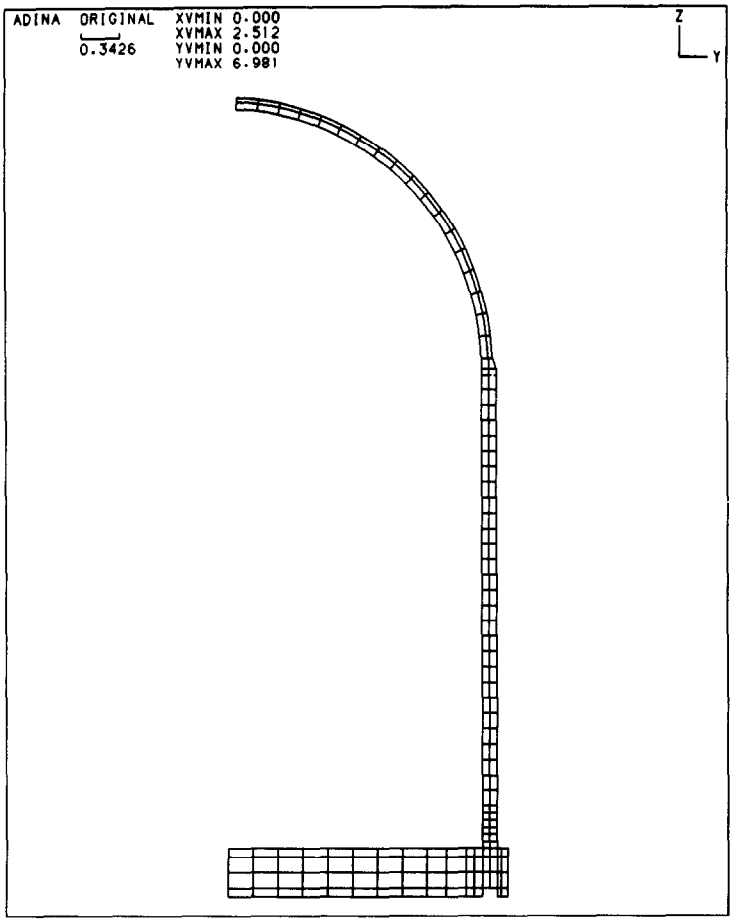

Fig. 32. Finite element mesh for the PWR containment model.

portion of the dome together with longitudinal tendons that cross the dome orthogonally in plane. The hoop tendons are anchored on three buttresses and the longitudinal tendons at the prestressing gallery below the base.

The model details are shown in Fig. 31 which follows closely the full size structure except for details in the bottom cap. The mesh used for the tenth scale model analysis is shown in Fig. 32. A similar mesh was employed on the full size structure, which was also being subjected to a more detailed analysis in which the element size was roughly halved throughout. A comparison of the two sets of results showed that for this structure the use of two elements through the wall was sufficient.

Figures 33 and 34 show progressive deflection behavior and crack build up at various pressure levels. The accuracy of these predictions will only be apparent after the forthcoming pressure tests but during the design process certain hand checks were made. One of these involved the radial displacement of the wall at mid-height which is sufficiently removed from the wall-base junction and the dome spring line as to make the behavior amenable to solution as a long cylinder.

During the pressurization process there are well defined stages at which the stress distribution could be calculated, these being during the early elastic period when the load is shared by the concrete, reinforcement and prestress, following the total cracking of the concrete with transfer of the load fully onto the reinforcement and prestress and finally after yielding of the reinforcement when the load is carried solely by the prestress. These conditions result in spot checks and are shown in Fig. 35 which plots the predicted radial deflection of the actual vessel at mid-height against the pressure. Close agreement is indicated with the ADINA analysis, the latter showing the effect of the post-tension stiffening during the period in which the load is transferred from the concrete onto the steel.

As in most analyses, there are areas of approximation and concern where known behavior has by necessity been ignored. In this analysis one such approximation is centered around the prestressing system. The three-dimensionality of the prestressing system both from the hoop and particularly in the meridional prestressing could be addressed by means of three-dimensional analyses although due to the various cyclic symmetries involved this may need to

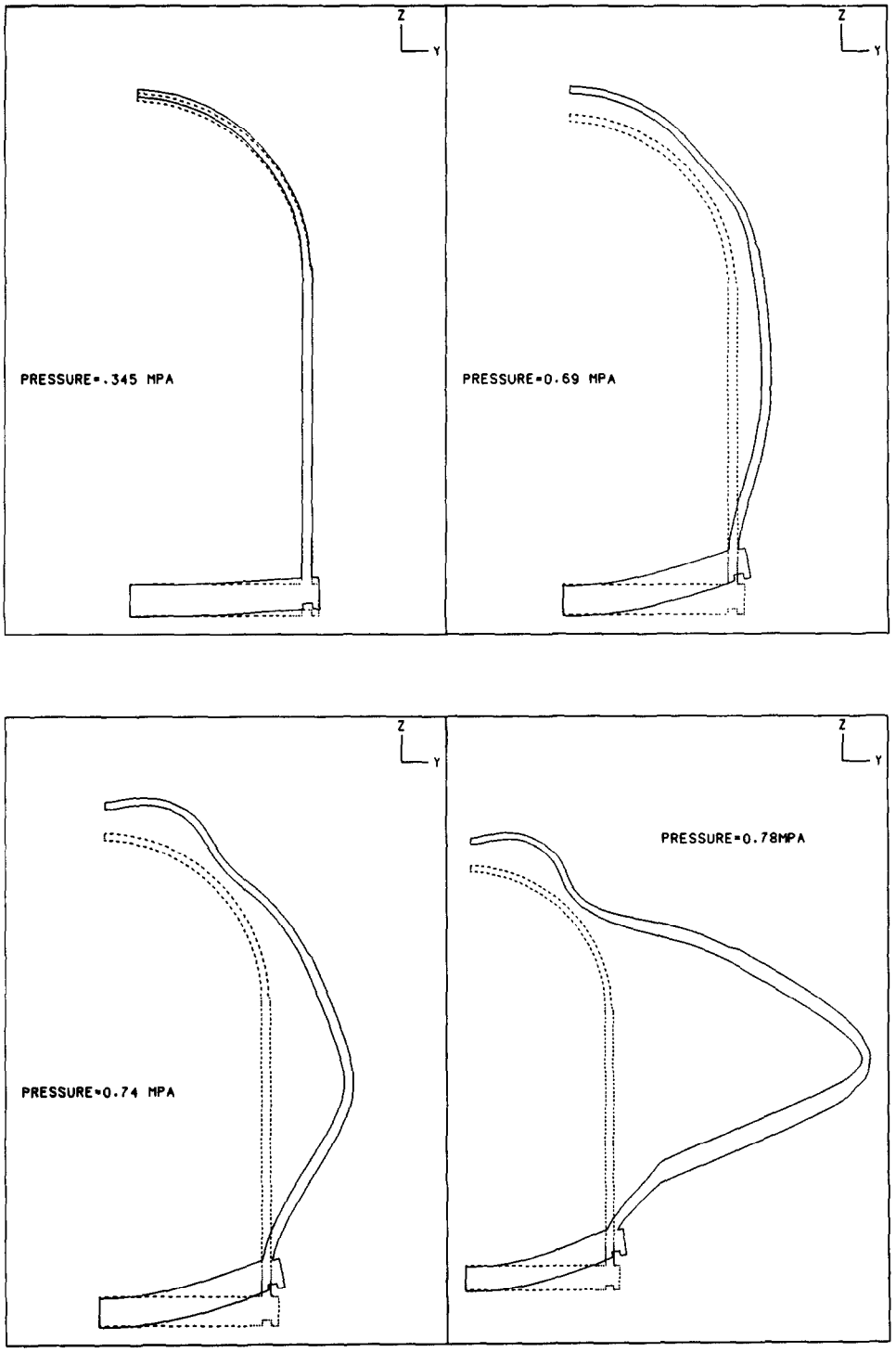

Fig. 33. Progressive deflection behavior at various pressure levels for the PWR containment model as predicted by ADINA. Displacements magnified by a factor of 66.

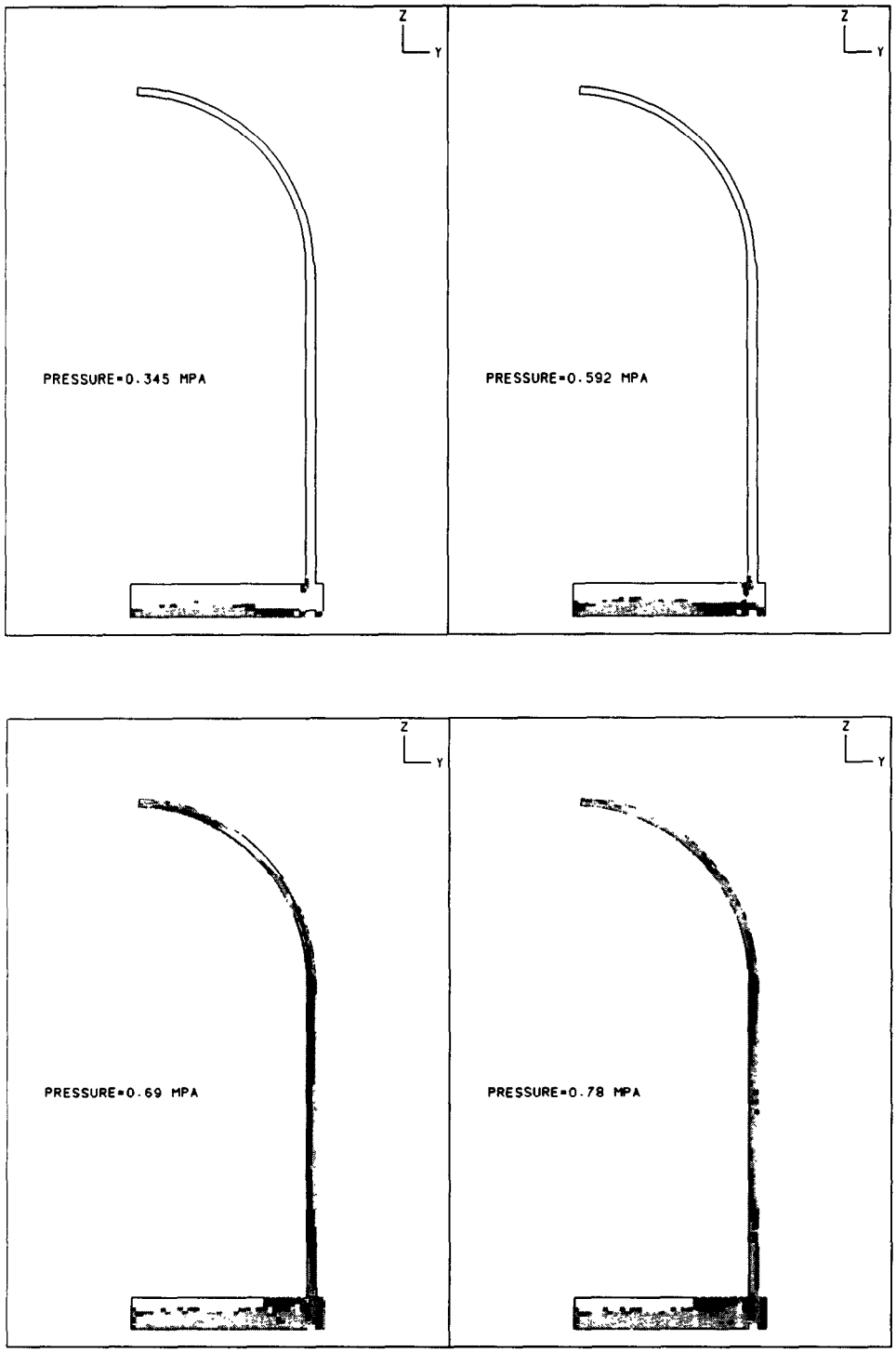

Fig. 34. Progressive crack build up at various pressure levels for the PWR containment model. In the original, yellow—1 crack, blue—2 cracks, red—3 cracks.

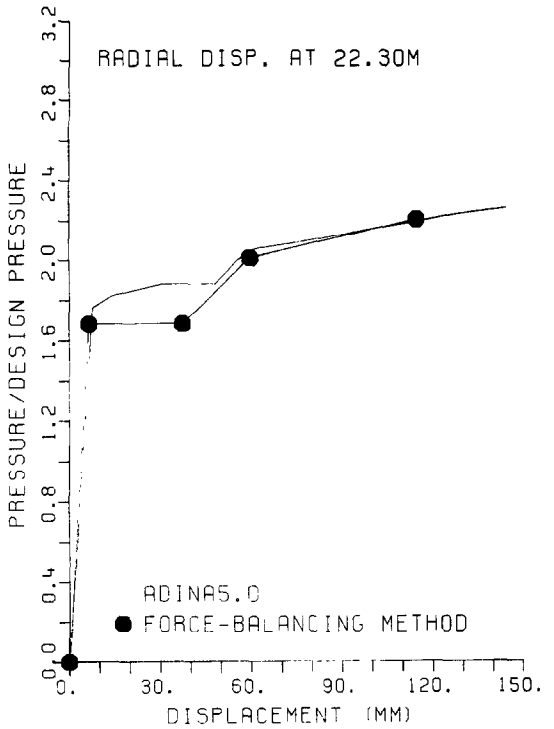

Fig. 35. Radial deflection of the PWR containment at mid-height as a function of applied pressure.

be at the best a 180° analysis and may even require a full 360° investigation. The test structure includes all the features of the main structure that could influence this and the need for a full three-dimensional analysis should be evident after the pressure test.

A more complicating feature in this instance is the fact that the prestress is unbonded. This is partly overcome for the vertical portion of the prestress as only end loads are considered but for the curved tendons the interaction between displacements and prestress forces is, whilst not being impossible, a very complex calculation. ADINA contains means of carrying this out as loads can be made deflection dependent and this has been demonstrated to be applicable to unbonded prestress, but the algorithm to cover the general situation is rather formidable.

3.4. *Discussion and conclusions*

The three structures detailed in the previous sections have helped to build up a high degree of confidence in the ADINA system and the concrete model. There is still the need of expertise in its successful application and there are areas that need further investigation. In particular the effect of more discrete cracks as would occur in mass concrete needs more study and from work (not yet published) involving explosive loadings, there is a need to model the concrete past the ultimate strain state as a compaction material. This may simply (Taylor Woodrow's word, not ADINA R & D's) involve marrying the concrete model with the Drucker–Prager cap model. Other topics for future consideration are solution strategies, especially with new automatic loading methods becoming available, bond between reinforcement and concrete and non-orthogonal cracking.

Concrete in all its many forms still remains a very complex material to model numerically but given the open exchange of ideas and mutual respect between code developers and structural analysts each successful application helps to meet tomorrow's challenges with an extra degree of confidence.

REFERENCES

1. K. J. Bathe, *Finite Element Procedures in Engineering Analysis*. Prentice–Hall, Englewood Cliffs, NJ (1982).
2. K. J. Bathe and S. Ramaswamy, On three-dimensional nonlinear analysis of concrete structures. *Nucl. Engng Des.* **52**, 385–409 (1979).
3. W. F. Chen, *Plasticity in Reinforced Concrete*. McGraw–Hill (1982).
4. Z. P. Bazant and J. C. Chern, Concrete creep at variable humidity: constitutive law and mechanisms. *Mater. Struct. RILEM.* **18**(103), 1–19 (1985).
5. S. Gallegos-Cazares and W. C. Schnobrich, Effects of creep on the behavior of reinforced concrete gable roof hyperbolic-paraboloids. Civil Engineering Studies, Structural Research Series No. 543, University of Illinois at Urbana-Champaign (1988).
6. H. Kupfer, H. K. Hilsdorf and H. Rusch, Behavior of concrete under biaxial stresses. *J. Am. Concr. Inst.* **66**, 656–666 (1969).
7. T. C. Liu, A. H. Nilson and F. O. Slate, Biaxial stress–strain relations for concrete. *J. Struct. Div., ASCE* **98**, 1025–1034 (1972).
8. M. H. Khan and B. Saugy, Concrete for nuclear reactors. Am. Concr. Inst. Special Publication **34** (1972).
9. P. Launay and H. Gachon, Concrete for nuclear reactors. Am. Concr. Inst. Special Publication **34** (1972).
10. J. S. Gedling, N. S. Mistry and A. K. Welch, Evaluation of material models for reinforced concrete structures. *Comput. Struct.* **24**, 225–232 (1986).
11. J. C. Pyle, Analysis of deep composite steel and concrete slabs. *Comput. Struct.* **13**, 661–671 (1981).
12. M. Keuser, B. Kepp, G. Mehlhorn and R. Rostasy, Nonlinear static analysis of end-fittings for GFRP prestressing rods. *Comput. Struct.* **17**, 719–730 (1983).
13. J. W. Tedesco and W. G. McDougal, Nonlinear dynamic analysis of concrete armor units. *Comput. Struct.* **21**, 189–201 (1985).
14. Z. P. Bazant, T. B. Belytschko and Ta-Peng Chang, Continuum theory for strain-softening. *J. Engng Mech. Div., ASCE* **110**, 1666–1692 (1984).
15. N. S. Mistry, Nonlinear analysis of reinforced concrete structures. *Finite Element News* **4** (1985).
16. D. B. Clauss, Round-robin pretest analyses of a 1:6 scale reinforced concrete containment model subject to static internal pressurisations. U.S. Nuclear Regulatory Commission NUREG/CR-4913, SAND87-0891 (1987).
17. S. Kloosterman, Validation report for the ADINA–TW finite element code. Report PWR/88/83, PMT Document SXB-IC-096064 (1988).
18. Task Committee on Finite Element Analysis of Reinforced Concrete Structures. A. H. Nilson, Chairman, State-of-the-art Report on Finite Element Analysis of Reinforced Concrete, ASCE Special Publication (1982).
19. Vejdirektoratet (Road Directorate, Ministry of Transport, Denmark), Load carrying capacity of bridges subjected to alkali–silica reactions. The shear strength of concrete beams subjected to ASR Interim Report No. 1 (1986).